The kinematics and excitation of infrared water vapor emission from planet-forming disks: results from spectrally resolved surveys and guidelines for JWST spectra

Banzatti, A.; Pontoppidan, K.M.; Pére Chávez, J.; Salyk, C.; Diehl, L.; Bruderer, S.; ... ; Wheeler, C.

The Astronomical Journal, 165:72 (30pp), 2023 February https://doi.org/10.3847/1538-3881/aca80b

The Kinematics and Excitation of Infrared Water Vapor Emission from Planet-forming Disks: Results from Spectrally Resolved Surveys and Guidelines for JWST Spectra

Andrea Banzatti[1], Klaus M. Pontoppidan[2], José Pérez Chávez[1], Colette Salyk[3], Lindsey Diehl[1], Simon Bruderer[4], Gregory J. Herczeg[5], Andres Carmona[6], Ilaria Pascucci[7], Sean Brittain[8], Stanley Jensen[8], Sierra Grant[4], Ewine F. van Dishoeck[4,9], Inga Kamp[10], Arthur D. Bosman[11], Karin I. Öberg[12], Geoff A. Blake[13], Michael R. Meyer[11], Eric Gaidos[14], Adwin Boogert[15], John T. Rayner[15], and Caleb Wheeler[16]
[1] Department of Physics, Texas State University, 749 N Comanche Street, San Marcos, TX 78666, USA; banzatti@txstate.edu
[2] Space Telescope Science Institute 3700 San Martin Drive Baltimore, MD 21218, USA
[3] Department of Physics and Astronomy, Vassar College, 124 Raymond Avenue, Poughkeepsie, NY 12604, USA
[4] Max-Planck-Institut für extraterrestrische Physik, Gießenbachstraße 1, D-85748 Garching bei München, Germany
[5] Kavli Institute for Astronomy and Astrophysics, Peking University, Beijing 100871, People's Republic of China
[6] Univ. Grenoble Alpes, CNRS, IPAG, F-38000 Grenoble, France
[7] Department of Planetary Sciences, University of Arizona, 1629 East University Boulevard, Tucson, AZ 85721, USA
[8] Department of Physics & Astronomy, 118 Kinard Laboratory, Clemson University, Clemson, SC 29634, USA
[9] Leiden Observatory, Leiden University, P.O. Box 9513, 2300 RA Leiden, The Netherlands
[10] Kapteyn Astronomical Institute, University of Groningen, PO Box 800, 9700 AV Groningen, The Netherlands
[11] Department of Astronomy, University of Michigan, 1085 S. University Avenue, Ann Arbor, MI 48109, USA
[12] Center for Astrophysics, Harvard Smithsonian, 60 Garden Street, Cambridge, MA 02138, USA
[13] Division of Geological & Planetary Sciences, MC 150-21, California Institute of Technology, Pasadena, CA 91125, USA
[14] Department of Earth Sciences, University of Hawaii at Manoa, 1680 East-West Road, Honolulu, HI 96822, USA
[15] Institute for Astronomy, University of Hawaii, 2680 Woodlawn Drive, Honolulu, HI, 96822 USA
[16] Simons Observatory—Center for Computational Astrophysics, Flatiron Institute, 162 5th Avenue, NY 10010, USA
Received 2022 September 16; revised 2022 November 15; accepted 2022 November 16; published 2023 January 26

Abstract

This work presents ground-based spectrally resolved water emission at $R = 30{,}000$–$100{,}000$ over infrared wavelengths covered by the JWST (2.9–12.8 μm). Two new surveys with iSHELL and the VISIR are combined with previous spectra from the CRIRES to cover parts of multiple rovibrational and rotational bands observable within telluric transmission bands, for a total of ≈160 spectra and 85 disks (30 of which are JWST targets in Cycle 1). The general expectation of a range of regions and excitation conditions traced by infrared water spectra is for the first time supported by the combined kinematics and excitation as spectrally resolved at multiple wavelengths. The main findings from this analysis are: (1) water lines are progressively narrower from the rovibrational bands at 2–9 μm to the rotational lines at 12 μm, and partly match broad and narrow emission components, respectively, as extracted from rovibrational CO spectra; (2) rotation diagrams of resolved water lines from upper-level energies of 4000–9500 K show vertical spread and curvatures indicative of optically thick emission (≈10^{18} cm^{-2}) from a range of excitation temperatures (≈800–1100 K); and (3) the new 5 μm spectra demonstrate that slab model fits to the rotational lines at >10 μm strongly overpredict the rovibrational emission bands at <9 μm, implying vibrational excitation not in thermodynamic equilibrium. We discuss these findings in the context of emission from a disk surface and a molecular inner disk wind, and provide a list of guidelines to support the analysis of spectrally unresolved JWST spectra.

Unified Astronomy Thesaurus concepts: Circumstellar disks (235); Protoplanetary disks (1300); Planet formation (1241); Exoplanet formation (492); Star formation (1569); Classical T Tauri stars (252); Herbig Ae/Be stars (723); Pre-main sequence stars (1290); High resolution spectroscopy (2096); Molecular spectroscopy (2095); Infrared astronomy (786); Vibrational spectroscopy (2249)

Supporting material: machine-readable tables

1. Introduction

The inner regions of young protoplanetary disks within ≈5–10 au from the central stars present the right conditions for molecular chemistry to thrive in a warm disk layer irradiated by stellar and accretion-shock radiations (e.g., Glassgold et al. 2009; Najita et al. 2011; Du & Bergin 2014; Walsh et al. 2015; Bosman et al. 2017; Woitke et al. 2018; Anderson et al. 2021). This inner molecular layer is observed through a forest of emission lines at infrared wavelengths from a number of molecules, especially from CO, H_2O, OH, HCN, C_2H_2, and CO_2 (e.g., Najita et al. 2003; Carr & Najita 2008; Salyk et al. 2008, 2011a; Pontoppidan et al. 2010a; Fedele et al. 2011; Mandell et al. 2012; Pascucci et al. 2013; Banzatti et al. 2017, 2022). These molecular spectra have been found to reflect the irradiation, physical, and chemical structure of inner disks through their excitation and kinematics. Line fluxes from different molecules present trends with stellar temperature (Pontoppidan et al. 2010a; Pascucci et al. 2013), with stellar and accretion luminosity (Salyk et al. 2011b; Brittain et al. 2016; Banzatti et al. 2017), with the formation of an inner disk dust cavity (Salyk et al. 2011b; Banzatti et al. 2017), and with

the dust disk mass and radius as observed at millimeter wavelengths (Najita et al. 2013; Banzatti et al. 2020). The line kinematics, when spectrally resolved in high-resolution spectra, reveal inner regions of gas depletion (Brittain et al. 2003; Salyk et al. 2009; Banzatti & Pontoppidan 2015), a different gas excitation in dust-free versus dust-rich regions (Brittain et al. 2007; van der Plas et al. 2015; Hein Bertelsen et al. 2016a; Banzatti et al. 2018), variability in line kinematics (e.g., Brittain et al. 2013; Banzatti et al. 2022), and kinematic profiles tracing both a disk surface in Keplerian rotation and a slow wind launched from inner disks (Bast et al. 2011; Pontoppidan et al. 2011; Brown et al. 2013; Banzatti et al. 2022). Infrared molecular spectra therefore provide fundamental diagnostics of the physics and chemistry of inner disks at the time of disk dissipation and planet formation.

Among the multiple molecules observed at infrared wavelengths, water presents unique opportunities and challenges. Water can be observed from molecular clouds, through the phases of star and planet formation, all the way to disks and exoplanets (e.g., van Dishoeck et al. 2014). Water is also expected to play a major role in planet formation from the dynamics (e.g., Ciesla & Cuzzi 2006), to the accretion of solids (e.g., Ros & Johansen 2013), to habitability (e.g., Krijt et al. 2022), and it is a major driver of exoplanet science today. However, the molecular structure of water, an asymmetric top molecule with three vibrational $(v_1\, v_2\, v_3)$[17] and three rotational $(J\, K_a\, K_c)$ quantum numbers, produces a complex rotational and rovibrational spectrum that spreads across infrared wavelengths, posing multiple technical challenges in observations (see Section 1.1) and in the analysis and interpretation of spectra (e.g., Meijerink et al. 2009; Kamp et al. 2013).

Observing water and its evolution in disks at the time of planet formation is one of the major drivers of scientific investigation in the field of planet formation with the James Webb Space Telescope (JWST), which is uniquely suited for water observations thanks to the wide spectral coverage, high sensitivity, and the location outside of Earth's atmosphere. Despite the amount of water spectra from disks collected to date (see previous summary in Banzatti et al. 2017), a number of fundamental questions remain:

1. which inner disk region(s) do the infrared water lines trace, and are there multiple water reservoirs (with different temperature and density);
2. what is the water abundance in inner disks and what determines it (chemistry versus dynamics);
3. what is the relative role of different excitation processes, and is water emission in local thermodynamic equilibrium (LTE);
4. is water present in a molecular inner disk wind; and
5. how can we correctly interpret the complex water spectra observed across infrared wavelengths within a unified picture of inner disks?

In this work we offer a contribution to this field at a time when the first water spectra are being observed with JWST (Yang et al. 2022). We present and analyze spectrally resolved water emission lines from rovibrational and rotational bands at multiple wavelengths between 2.9 and 12.9 μm tracing upper-level energies between 4000 and 9500 K, and compare them to the velocity and excitation of rovibrational CO spectra observed at 4.5–5.25 μm tracing the same range in upper-level energies. One goal of this work is to present guidelines to support the analysis of both individual and large samples of spectrally unresolved water spectra from JWST.

[17] For symmetric stretching, bending, and asymmetric stretching modes, respectively.

1.1. Observing Water in Disks: The Need for a Synergy between Space and Ground Data

Water spectra in protoplanetary disks have so far been observed with instruments that fall under two main categories: space-based low-resolution spectrographs (e.g., IRS on Spitzer with maximum resolving power $R \approx 700$), and ground-based high-resolution echelle spectrographs (e.g., Cryogenic Infrared Echelle Spectrometer (CRIRES) on the Very Large Telescope (VLT) with $R \approx 95{,}000$). Each type of instrument presents specific advantages and disadvantages, which we illustrate in Figure 1. Space-based spectrographs provide wide spectral coverage (e.g., 10–37 μm with Spitzer-IRS, and now 4.9–28 μm with JWST-MIRI) but lose kinematic information on the observed emission, and blend together lines from multiple emission/absorption components and different chemical species. Conversely, ground-based spectrographs provide high resolving power that separates the emission from different lines and molecules and reveals the gas kinematics in high detail, but they can only observe in limited spectral windows of higher telluric transmission within the L, M, and N bands (Figure 1 and Table 1).

In Figure 1 we report a water emission model for quick guidance on the structure of the spectrum across wavelengths. The model is described below in Section 4.3, and in this figure we use a temperature of 700 K, column density of 10^{18} cm^{-2}, and line FWHM of 15 km s^{-1}. We visually scale the model to approximately match the observed emission in DR Tau just for line identification (in Section 4.4 we will present actual model fits to the data). Purely rotational lines populate a large part of the spectrum at wavelengths longer than 10 μm, while rovibrational transitions in the bending and stretching modes present more compact bands at 4–9 μm and 2.5–3.5 μm, respectively. We include in the figure a sky transmission spectrum as obtained from the ESO SkyCalc application, set up for the Paranal site (altitude of 2640 m) and using airmass = 1 and precipitable water vapor (PWV) = 2.5 mm. Comparison of Earth's transmission to the water emission spectrum in the top two panels in Figure 1 demonstrates that ground-based instruments enable observations of the water spectrum only where it is relatively weak (the tails of rovibrational bands and a few rotational lines near 12.4 μm).

Using observations from space or from the ground, previous work has therefore focused on data sets or samples that were limited one way or the other, resulting in an incomplete view of the distribution and excitation of water in inner disks. Some studies analyzed large samples (up to ≈100 objects) of spectrally unresolved rotational water emission observed with Spitzer-IRS at 10–37 μm or Herschel-PACS/HIFI at 50–540 μm; due to the low resolving power and blending of emission lines, Spitzer spectra only provided degenerate model solutions for the properties (temperature and column density) of multiple molecules and no direct kinematic information on the radial location of emitting regions (Carr & Najita 2011; Salyk et al. 2011b; Pascucci et al. 2013), while Herschel observations provided very low detection rates of a few lines only (e.g., Riviere-Marichalar et al. 2012; Du et al. 2017).

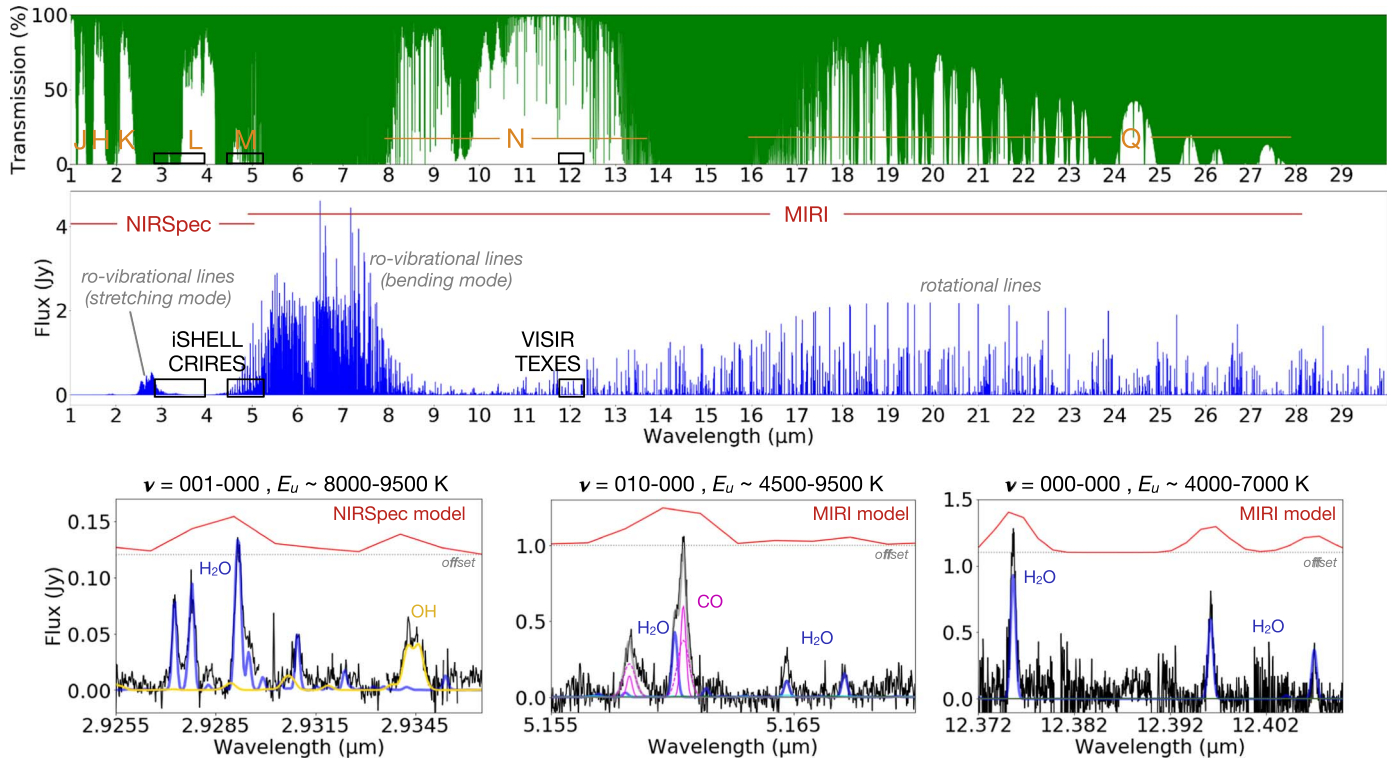

Figure 1. Overview of near- and mid-infrared water emission bands as observed from space and the ground (see Section 1.1). Top: Earth's atmospheric transmission (in green), with observing bands labeled in orange. Middle: water emission model for illustration of its multiband structure (not a fit to the data; model fits to the data are instead shown in Sections 2 and 4.4). The coverage of different spectrographs is shown with black boxes to illustrate which parts of the spectrum can be observed: high-resolution ($R > 30{,}000$) spectrographs from the ground can spectrally resolve relatively weak high-energy lines in small spectral windows, while JWST from space can observe a much wider spectral range but only at moderate resolution ($R \sim 1500$–3700). Bottom: zoomed-in spectral regions to illustrate the difference in resolution between JWST and ground-based data (the CRIRES, iSHELL, and TEXES spectra are for DR Tau and adopted from this work, Banzatti et al. 2017, and Salyk et al. 2019).

Table 1
Summary of High-resolution Water Spectra Observed in Disks with Four Ground-based Instruments

λ (μm)	Instrument	R	# Lines	E_u (K)	$n_{\rm crit}$ (cm^{-3})	Sample (# disks)	Detections (# disks)	References
2.9–2.98	CRIRES	95,000	≈25	8000–9500	10^{15}–10^{16}	46	16	1
4.52–5.24	iSHELL	60,000	≈40	4500–9500	≈10^{13}	60	10	this work, 2
12.23–12.87	VISIR	30,000	2–11	3200–7000	≈10^{11}	64	10	this work
12.37–12.46	TEXES	100,000	3–7	3600–6000	≈10^{11}	9	7	3

Note. Critical densities $n_{\rm crit} = A_{ul}/C_{ul}$ are estimated using molecular data adopted in RADEX (see Section 4.3). As collision temperature, we use the excitation temperatures from Table 3. Since upper-level energies E_u only up to 7200 K are included in Faure & Josselin (2008), as collisional rates C_{ul} for the 2.9–2.98 μm lines, we take those of lines near 2.7 μm with the same range in A_{ul} but E_u of 6000–7200 K.

References. 1: Banzatti et al. (2015, 2017), Mandell et al. (2012), Fedele et al. (2011), and Salyk et al. (2022); 2: Banzatti et al. (2022); 3: Najita et al. (2018) and Salyk et al. (2019). Additional high-resolution water spectra from CSHELL and NIRSPEC have been published in Carr et al. (2004), Salyk et al. (2008), and Doppmann et al. (2011).

Other studies analyzed small samples of high-resolution spectra from the ground, mostly biased toward highly accreting disks that had been observed with Spitzer to have strong water emission; these spectra provided first kinematic information on the water emission but were very limited in sensitivity and by strong telluric absorption (Pontoppidan et al. 2010b; Salyk et al. 2019) and, in the case of the 2.9 μm water band, by absorption in stellar photospheres (Banzatti et al. 2017). The properties of water emission as observed in different samples and different wavelengths have ranged from high temperatures in very optically thick regions in the L band ($T \approx 1500$ K and $N \approx 10^{20}$ cm^{-2}, found in only three disks so far; Carr et al. 2004; Doppmann et al. 2011; Salyk et al. 2022), to moderate temperatures and opacity in a narrow window in the N band ($T \approx 500$–700 K and $N \approx 10^{18}$ cm^{-2}; Najita et al. 2018; Salyk et al. 2019), down to cooler temperatures at mid- and far-infrared wavelengths (300–600 K; Carr & Najita 2011; Salyk et al. 2011b; Riviere-Marichalar et al. 2012; Liu et al. 2019). Apart from those analyzing Spitzer spectra, previous results were always based on small samples of 1–10 bright sources.

Supporting the scenario of water emitting from a radial range of disk regions, the combined analysis of spectrally unresolved mid- and far-infrared water spectra has suggested that water emission should come from disk surfaces from the dust sublimation radius out to 10 au or even larger radii (e.g., Antonellini et al. 2015; Blevins et al. 2016; Notsu et al. 2016; Woitke et al. 2018), where different emission lines probe a range of disk regions and layers depending on their upper-level

energy and Einstein-A coefficient. However, a unified picture of water in inner disks across different emission bands, including the rovibrational lines in the near-infrared and calibrated on spectrally resolved water line kinematics, is still lacking. JWST now covers both the rotational lines at >10 μm ($E_u \approx 1000$–6000 K) and the rovibrational lines from the bending mode ($E_u \approx 4000$–$10{,}000$ K) simultaneously and at similar resolving power ($R = 1500$–3700 across Mid-Infrared Instrument, MIRI, wavelengths), providing unprecedented leverage on the excitation of water across inner disk radii. One goal of this paper is to support the analysis of JWST spectra by providing spectrally resolved line kinematics at multiple wavelengths from a suite of high-resolution ground-based spectrographs (Table 1). A comprehensive view of water in disks will require the combination of multiple instruments from the ground and space at least until a space-based infrared telescope with high resolving power ($R >30{,}000$) is possibly built (e.g., Pontoppidan et al. 2018; Kamp et al. 2021).

2. Spectra Included in This Work

Table 1 reports the samples of water spectra available from four high-resolution ground-based instruments and some properties of the water emission they cover. Each data set is described in the next sections instrument by instrument; the data newly presented in this work come from two separate surveys performed with the VLT Imager and Spectrometer for the Mid-Infrared (VISIR) and iSHELL, while the CRIRES water spectra (Banzatti et al. 2017) and TEXES water spectra (Najita et al. 2018; Salyk et al. 2019) were published before. All of the reduced, science-ready spectra from CRIRES, VISIR, and iSHELL are available on www.spexodisks.com (Perez Chavez et al. 2021; C. Wheeler et al. 2023, in preparation). A list of the most prominent water lines covered in these spectra is reported in Table 2. A gallery of portions of the water spectra at multiple wavelengths object by object is included in Appendix A. Throughout this paper, spectra and spectral lines are shown in the heliocentric reference frame as corrected for the barycentric velocity at the time of observation of each target.

2.1. VLT-CRIRES Spectra at 2.9 μm

Water rovibrational emission spectra at 2.9–2.98 μm are included as observed with CRIRES (Kaeufl et al. 2004) on VLT as part of a survey from 2007–2008 (European Southern Observatory, ESO, Large Program 179.C-0151; Pontoppidan et al. 2011; Brown et al. 2013). The water spectra were obtained for ≈50% of the sample in that survey (35 out of 69 disks, mostly T Tauri stars) and were presented and analyzed in Banzatti et al. (2017), except for the very different spectrum with a much larger number of high-excitation lines observed in VV CrA S, which is published in Salyk et al. (2022). Additional spectra for 11 Herbig Ae/Be stars were presented in Fedele et al. (2011).

The T Tauri spectra included in this work were taken with a resolving power of ≈95,000 or ≈3 km s^{-1}, and most of them required correction for stellar photospheric absorption on top of telluric correction. The observed water emission lines were found to be generally as broad as the broad component of CO M-band emission (FWHM up to ≈100 km s^{-1} in some disks), and in a few cases to include also weak narrower central emission similar to the kinematic structure of CO (for details, see Banzatti et al. 2017). An example L-band spectrum from CRIRES is shown in Figure 2, showing ≈15–20 prominent water lines that in some cases are blends of two nearby transitions (the blending of lines increases with line broadening, and is generally more severe than in the example shown here; see Figure 14 in Banzatti et al. 2017).

Table 2
List of Prominent H_2O Lines Covered in This Work

Wavelength (μm)	Transition (Upper-lower Levels) (Level Format: $v_1v_2v_3$ $J_{K_aK_c}$)	A_{ul} (s^{-1})	E_u (K)
2.90813	001-000 $14_{0\,14} - 15_{0\,15}$	48.4	8341
2.90829	001-000 $11_{4\,8} - 12_{4\,9}$	42.5	8004
2.90911	001-000 $10_{6\,4} - 11_{6\,5}$	31.8	8031
2.90998	001-000 $12_{2\,10} - 13_{2\,11}$	48.8	8177
2.91012	001-000 $13_{2\,12} - 14_{2\,13}$	48.8	8293
2.92726	001-000 $15_{1\,15} - 16_{1\,16}$	49.5	8744
2.92726	001-000 $15_{0\,15} - 16_{0\,16}$	48.9	8744
2.92780	001-000 $12_{3\,9} - 13_{3\,10}$	51.6	8388
2.92912	001-000 $13_{3\,11} - 14_{3\,12}$	48.3	8583
2.92920	001-000 $14_{1\,13} - 15_{1\,14}$	48.7	8698
2.93096	001-000 $11_{6\,6} - 12_{6\,7}$	33.6	8411
2.94665	001-000 $16_{0\,16} - 17_{0\,17}$	48.9	9172
2.94861	001-000 $14_{2\,12} - 15_{2\,13}$	48.9	9012
4.72810	010-000 $9_{7\,2} - 8_{6\,3}$[a]	2.4	5074
4.72942	010-000 $11_{6\,5} - 10_{5\,6}$[a]	2.1	5515
4.79063	001-000 $10_{6\,5} - 9_{5\,4}$[a]	2.6	5129
4.84063	010-000 $9_{6\,3} - 8_{5\,4}$	2.6	4778
4.88205	010-000 $20_{3\,18} - 19_{2\,17}$	10.6	9179
4.91324	010-000 $22_{2\,21} - 21_{1\,20}$	14.3	9864
4.95058	020-010 $9_{5\,4} - 8_{4\,5}$	4.7	6884
4.96548	010-000 $16_{4\,13} - 15_{3\,12}$	6.7	7329
4.99774	020-010 $6_{6\,1} - 5_{5\,0}$	19.0	6341
5.00798	010-000 $15_{4\,12} - 14_{3\,11}$	6.2	6814
5.03885	010-000 $19_{1\,18} - 18_{2\,17}$[a]	14.5	8103
5.06240	010-000 $16_{3\,14} - 15_{2\,13}$[a]	9.6	6975
5.06429	010-000 $16_{2\,14} - 15_{3\,13}$	9.5	6974
5.07548	020-010 $7_{5\,2} - 6_{4\,3}$	5.9	6286
5.10815	010-000 $12_{4\,9} - 11_{3\,8}$[a]	4.2	5425
5.11080	010-000 $5_{3\,13} - 14_{2\,12}$[a]	9.1	6485
5.13018	010-000 $11_{4\,8} - 10_{3\,7}$	3.7	5018
5.16471	010-000 $20_{1\,20} - 19_{0\,19}$[a]	18.2	8074
5.16709	010-000 $14_{2\,12} - 13_{3\,11}$	8.6	6019
5.22140	010-000 $15_{1\,14} - 14_{2\,13}$	12.4	6105
5.22307	010-000 $13_{2\,11} - 12_{3\,10}$	8.0	5578
12.2481	000-000 $17_{5\,13} - 16_{2\,14}$	7.8	5795
12.2654	000-000 $18_{7\,12} - 17_{4\,13}$	12.3	6954
12.2772	000-000 $12_{8\,5} - 11_{5\,6}$	0.5	4048
12.2876	000-000 $9_{9\,1} - 8_{6\,2}$	0.02	3202
12.3757	000-000 $16_{4\,13} - 15_{1\,14}$	4.2	4948
12.3962	000-000 $17_{4\,13} - 16_{3\,14}$	7.7	5781
12.4070	000-000 $16_{3\,13} - 15_{2\,14}$	4.2	4945
12.4448	000-000 $11_{8\,3} - 10_{5\,6}$	0.3	3629
12.4535	000-000 $13_{7\,6} - 12_{4\,9}$	1.2	4213
12.8319	000-000 $10_{8\,2} - 9_{5\,5}$	0.2	3243
12.8702	000-000 $10_{8\,3} - 9_{5\,4}$	0.2	3243

Note. Line properties are from HITRAN (Gordon et al. 2022).
[a] = lines used for stacking.

2.2. IRTF-iSHELL Spectra at 5 μm

Water rovibrational emission spectra at 5 μm are included as observed with iSHELL (Rayner et al. 2016, 2022) at the NASA Infrared Telescope Facility (IRTF), as part of an ongoing

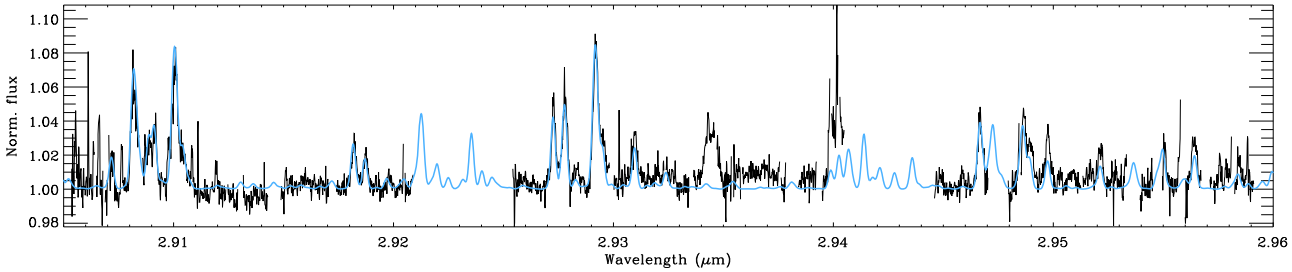

Figure 2. Example of a CRIRES *L*-band spectrum, for the disk of DR Tau (from Banzatti et al. 2017). A water emission spectrum is shown in light blue, using the LTE slab model fit described in Section 4.4. The prominent feature near 2.935 μm is an OH doublet.

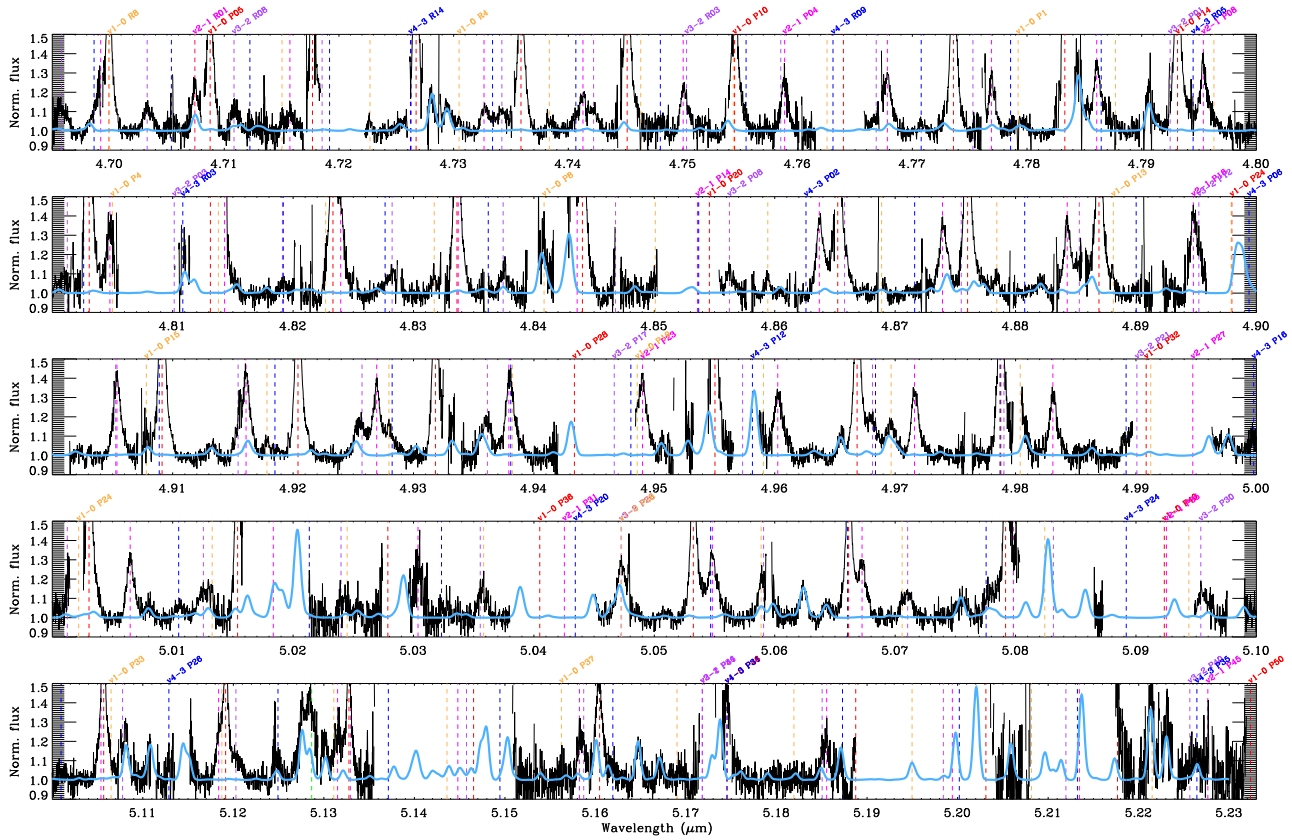

Figure 3. Example of part of an iSHELL *M*-band spectrum, for the disk of FZ Tau. A water emission spectrum is shown in light blue, using the LTE slab model fit described in Section 4.4. CO lines are marked in other colors (^{13}CO in orange, all other colors for ^{12}CO) and labeled for reference, but the plot zooms in on the water lines for better visualization of these and cuts off the peaks of $v = 1 - 0$ CO lines. H I emission from the Hu δ line blended with water near 5.13 μm is marked in light green.

M-band survey of protoplanetary disks (Banzatti et al. 2022). iSHELL covers a wide portion of the observable *M* band at 4.5–5.25 μm in one shot, with only narrow gaps between the echelle orders at longer wavelengths, providing simultaneous observations of CO, H_2O, and H I (Banzatti et al. 2022). Most spectra were taken with the 0.″75 slit and a resolving power of ≈60,000 or ≈5 km s^{-1}, while the narrower slit with ≈92,000 or ≈3.3 km s^{-1} was used only for the brightest disks (mostly around Herbig Ae/Be stars, where water is not detected). The iSHELL spectra included here were reduced with Spextool v5.0.3 (Cushing et al. 2004) and have been presented in Banzatti et al. (2022) or obtained in 2022 January–July, for a total current sample of 60 disks. Multiepoch observations have been obtained for some disks and show variability (e.g., Figure 8 in Banzatti et al. 2022); in this work, we only include one epoch, and we will study the variability in a future publication.

The *M*-band water lines have been discovered in the disk of AS 205 N and reported for the first time in Banzatti et al. (2022), and in this new work we include all of the current detections from the rest of the survey. An example is presented in Figure 3. In the currently available *M*-band spectra, a total of ≈40 rovibrational water lines are observed (mostly from $v = 1$ and some from $v = 2$, see Table 2), some of which are blended with CO or H I emission. In this work, we make a weighted average of eight water lines that are not blended with CO to produce a stacked velocity profile with higher signal-to-noise ratio (S/N); these lines are marked in Table 2. At the S/N obtained in these spectra, the *M*-band water lines are consistent with having the same velocity profile; future higher-sensitivity spectra could be used to test for any change in rovibrational line profiles as a function of E_u.

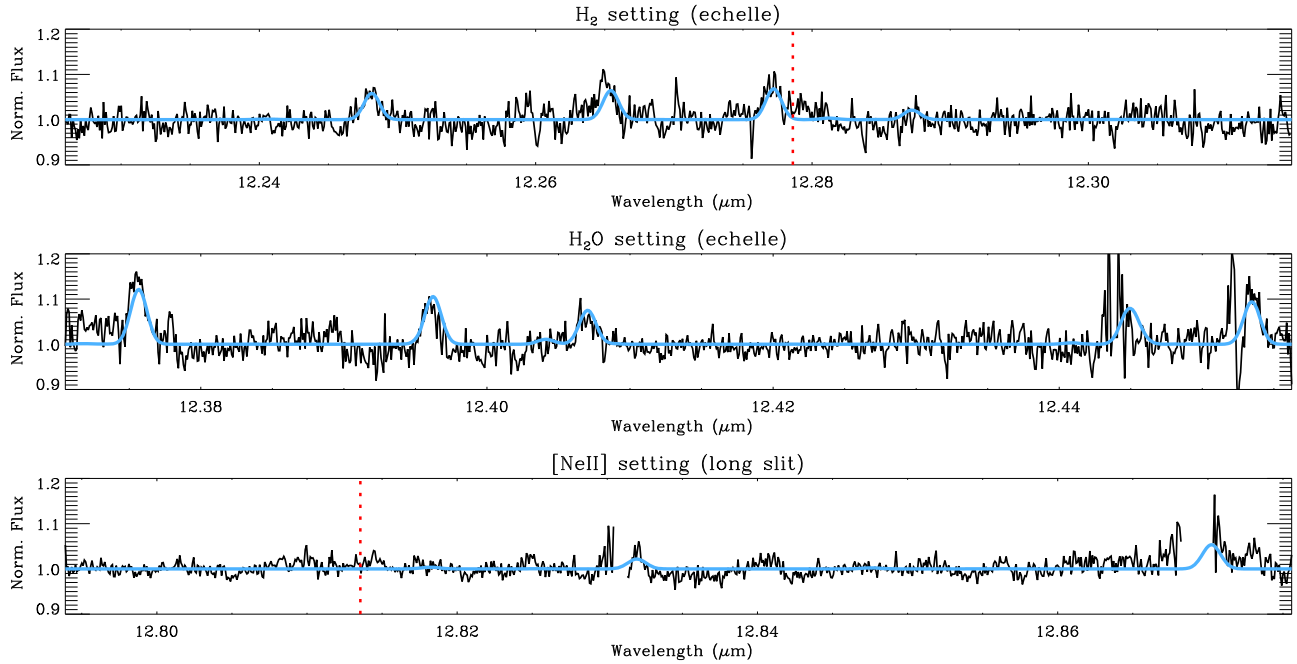

Figure 4. Example of all three spectral settings from the VISIR survey, for the disk of CrA-IRS2 (CHLT 1). Up to 11 water lines are covered, and up to seven are detected in this survey. Water lines near 12.85 μm are from levels with upper-level energies 3200 K, and could not be corrected from the deep and broad telluric lines (see Appendix B). A water emission spectrum is shown in light blue, using the LTE slab model fit described in Section 4.4. The positions of [Ne II] and H_2 lines are marked with dotted lines (neither is detected in this spectrum).

2.3. VLT-VISIR Spectra at 12.4 μm

Water rotational emission spectra at 12.2–12.9 μm were obtained within a Large Program with VISIR (Lagage et al. 2004), and are presented and analyzed in this work for the first time. This survey used VISIR at the VLT right after its upgrade (Käufl et al. 2015) and over semesters between 2016 August and 2018 August (program IDs 095.C-0203 and 198.C-0104, PI: K. Pontoppidan). A spectrum is shown in Figure 4 as an example.

The survey included three settings: two echelle settings centered at 12.27 and 12.41 μm to cover emission from H_2O lines and the 0-0 S(2) H_2 line at 12.2786 μm (and possibly OH), and one long-slit setting centered at 12.84 μm to include the [Ne II] line at 12.8136 μm and two water lines with upper-level energy 3200 K. The central wavelengths of all settings were set to maximize the number of H_2O emission lines to be observed, a total of 11 (Table 2). We used the 0.″75 slit providing a resolving power $R \approx 30{,}000$ (or 10 km s^{-1}). The data reduction is based on a custom pipeline initially made for VISIR 1 data (Banzatti et al. 2014) and adapted to the upgraded VISIR. Appendix B reports more details on the observations and reduction.

The total numbers of spectra obtained in each setting, including multiple epochs and/or slit orientations for a given target, are: 60 spectra in the H_2O setting, 16 spectra in the H_2 setting, and 45 spectra in the [Ne II] setting. Out of 64 targets, 22 were observed in at least two settings, and four targets were observed in all three settings (CrA-IRS2, SCrA, TCrA, and VVCrA; see Appendix B). To increase S/N, we have combined by weighted average spectra from multiple epochs and/or slit orientations obtaining one spectrum per object per setting. In the case of DR Tau, we averaged three epochs of data obtained earlier in program 088.C-0666 at higher S/N (Banzatti et al. 2014). The [Ne II] detections obtained in this survey have been presented and analyzed in Pascucci et al. (2020); H_2O and [Ne II] detections overlap in two disks only, RU Lup and VW Cha, but the lines have very different kinematic structure where [Ne II] only traces gas at high blueshifted velocities of -50 to -200 km s^{-1} in these two systems. No H_2 detections are reported from this survey, consistent with previous low detection rates (Bitner et al. 2008; Carmona et al. 2008).

2.4. Gemini-TEXES Spectra at 12.4 μm

Additional water rotational emission spectra at 12.2–12.4 μm are included as obtained with TEXES on Gemini (Lacy et al. 2002) with a resolving power of 100,000 or 3 km s^{-1} and previously presented in Najita et al. (2018) and Salyk et al. (2019). In this work we consider only the highest S/N among these spectra, obtained in four disks (see Section 4.1).

3. Sample

The sample included in this work is the combination of samples from the different programs described above as obtained with each instrument. The total is 85 protoplanetary disks around pre-main-sequence stars with temperatures of 3000–20,000 K and masses of 0.4–5 $M_\odot$ (i.e., including both T Tauri and Herbig Ae/Be stars) in nearby star-forming regions (mostly within ≈200 pc). Accretion luminosities are in the range of 0.01–200 $L_\odot$ and millimeter disk radii of 10–200 au, including a number of disks with inner dust cavities (here traced using the infrared index n_{13-30}; see Brown et al. 2007; Furlan et al. 2009; Banzatti et al. 2020) and some disks in wide multiple systems (see Section 3.1). The sample is listed in full in Appendix C and sample properties are visualized in Section 4.2. Out of ≈70 disks planned for observations with

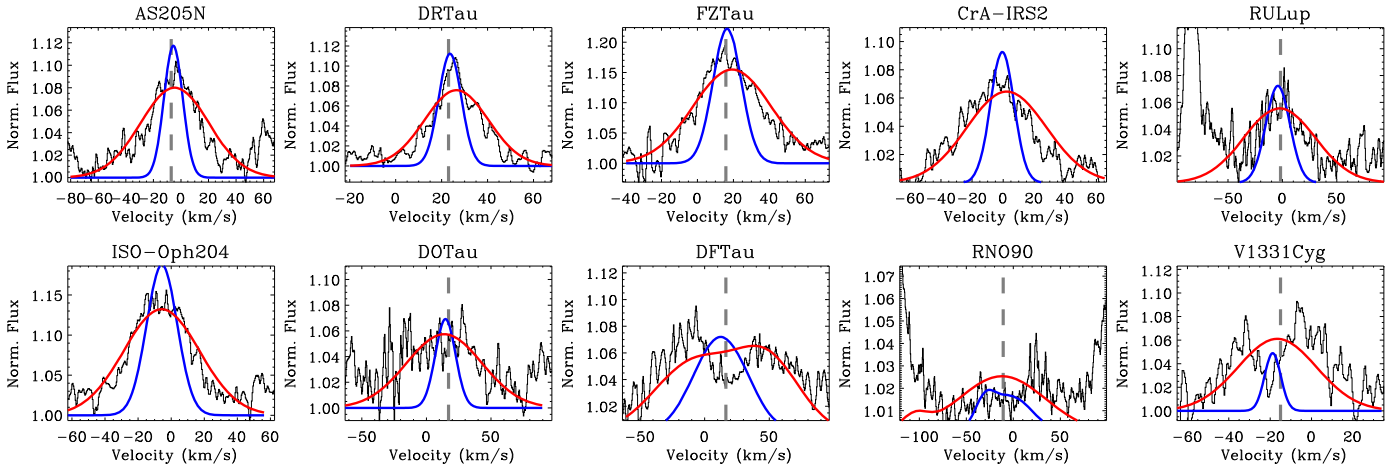

Figure 5. Gallery of H_2O detections in iSHELL spectra near 5 μm, using the stacked line profile (see Section 2.2). CO line components are scaled to match the relative strength of water lines for visual comparison, with the BC in red and the NC in blue. Spectral lines are shown in heliocentric velocity, and stellar RVs are marked with vertical dashed lines, where available.

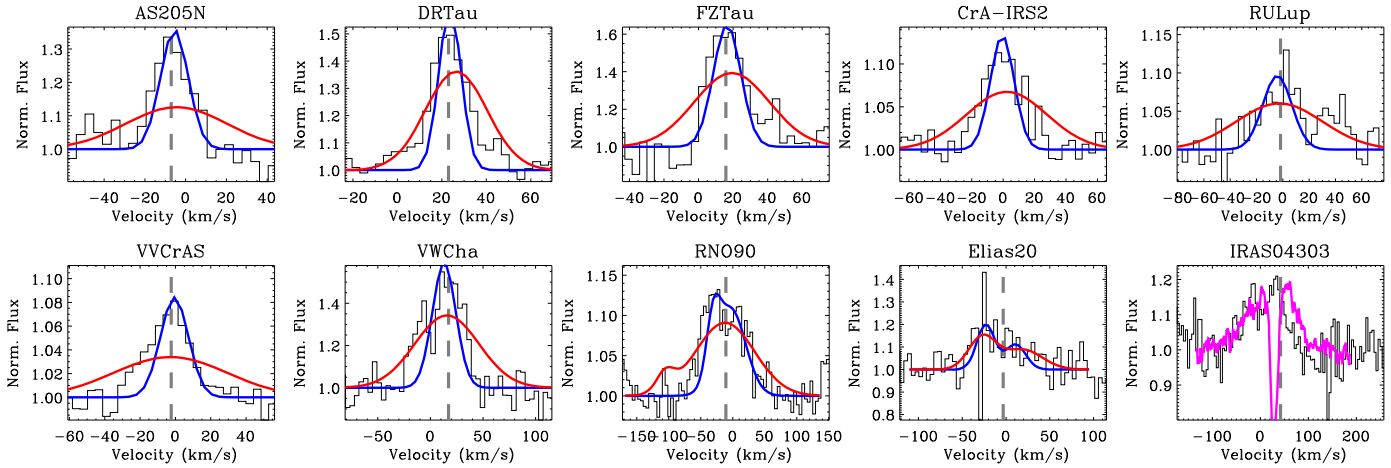

Figure 6. Gallery of H_2O detections in VISIR spectra, using the 12.396 μm line that is the least affected by telluric absorption (see Figure 22). CO components and stellar RVs are marked as in Figure 5. Due to the deep and broad absorption, CO components are not extracted in IRAS 04303, and the full observed line profile is shown instead.

JWST-MIRI in Cycle 1, 30 have high-resolution spectra that are included in this work.

3.1. Wide Multiple Systems

There are some wide multiple systems in the sample (e.g., Prato et al. 2003; Manara et al. 2019; Panić et al. 2021): AS 205 (separation 1.″3), DoAr 24E (GSS 31, 2.″2), S CrA (1.″3), VV CrA (1.″9), DK Tau (2.″4), UY Aur (0.″9), *T* Tau (0.″7), and KK Oph (1.″6). In good seeing conditions, we aligned the slit along the system axes so that the main binary components could be extracted. AS 205 A is the brighter component in the north, AS 205 B the fainter component in the south. DoAr 24E A is the brighter component in the north, but it becomes fainter than the B component in the south in the *L* band and at longer wavelengths (Prato et al. 2003; Brown et al. 2013). Therefore, in our data, DoAr 24E B (S) is the brighter component. SCrA A is the brighter component in the northwest, SCrA B is the fainter component in the southeast; VVCrA A is the brighter component in the south, VVCrA B is the fainter component in the north (Sullivan et al. 2019a). DK Tau A, UY Aur A, *T* Tau A, and KK Oph A are the brighter components in the north in each system (e.g., Manara et al. 2019; Panić et al. 2021).

4. Analysis

4.1. H_2O Line Kinematics

The first point we address in this work is about the line kinematics and emitting regions of water as spectrally resolved at multiple wavelengths, addressing questions (1) and (4) listed in Section 1. Previous work found that 2.9 μm lines are dominated by a broad emission component that matches the width of the broad component in CO emission lines in the same systems (Banzatti et al. 2017). At 12.4 μm, instead, line velocities were found to be narrower and match the narrow component in CO emission in a few disks where data was available (Banzatti et al. 2017; Salyk et al. 2019). With the new surveys and larger sample included in this work, it is now possible to expand the comparison between CO emission components and water emission lines on a larger number of detections and, for the first time, including water emission in the *M* band around 5 μm.

Figures 5 and 6 show a comparison of the H_2O line profiles using the CO line profiles observed in each object as reference.

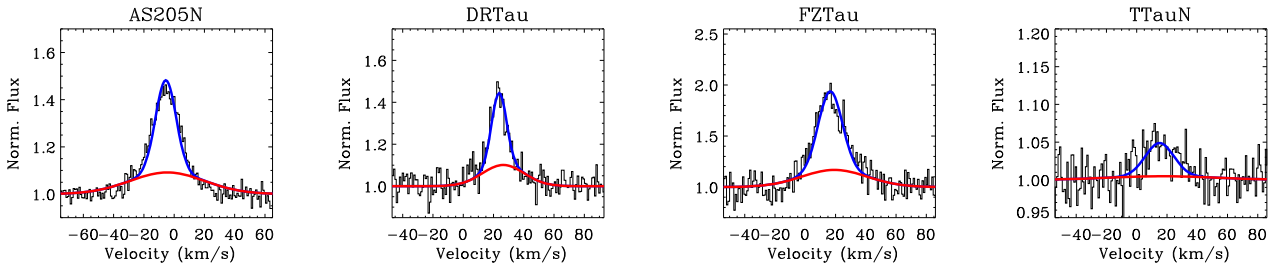

Figure 7. Two-Gaussian fits to the 12.396 μm water line in TEXES spectra using the BC and NC CO components in each disk.

Line profiles from the fundamental $v = 1 - 0$ lines have been observed with VLT-CRIRES and IRTF-iSHELL (Pontoppidan et al. 2011; Brown et al. 2013; Banzatti et al. 2022), and have been decomposed into broad BC and narrow NC velocity components as described in Banzatti & Pontoppidan (2015) and Banzatti et al. (2022). Gaussian fits to these two components are then scaled to match the relative strength of water lines to visualize the broadening of water relative to each CO component. The 10 iSHELL spectra where H_2O is detected show that the kinematic profile of H_2O emission at 5 μm is broader than the NC but narrower than the BC in at least six out of 10 cases. In the other four cases (DO Tau, DF Tau, RNO 90, and V1331 Cyg), water lines are as broad as the BC. In DF Tau, and tentatively in RNO 90 too, water shows a double-peaked shape that matches the width of the BC. In V1331 Cyg, water is as broad as the BC and possibly has a narrower blueshifted absorption (see also Section 4.1.1); its near-infrared spectrum is overall more complex due to an uncommonly high excitation of both CO and water (see the *L*-band water spectrum in Doppmann et al. 2011), and will be analyzed in detail in a future work. Additional tentative detections are found in three more disks (UY Aur A, Elias 24, and HD 35929), which are all included in the plots in Appendix A.

The 10 H_2O lines detected in the VISIR spectra show that the kinematic profile of H_2O emission at 12.4 μm is rather well matched by the narrow CO component in six out of 10 cases, within the uncertainty of the much lower pixel sampling and resolution of the VISIR spectra. The comparison between CO and H_2O lines is ambiguous in two cases (RU Lup and Elias 20), due to the low S/N of the water spectra. The case of VW Cha shows a broader water line with potentially a blueshifted absorption, which will be discussed in Section 4.1.1. The case of IRAS 04303 shows a very broad water line, similarly broad as the CO line; in this case, Figure 6 shows the complete CO line profile as observed, rather than decomposed into BC and NC as in the other objects, to illustrate the presence of a broad, deep, and blueshifted absorption component in the CO line (which is detected up to P38; i.e., this is another one of the highly excited blueshifted absorption spectra reported in Banzatti et al. 2022).

In Figure 7 we show fits to the 12.396 μm water emission line observed in the four highest-quality TEXES spectra from Najita et al. (2018) and Salyk et al. (2019). Water was detected in three more disks in Salyk et al. (2019), DoAr 44, HL Tau, and RW Aur, but with too low of S/Ns to apply this analysis. Given the higher resolution and S/Ns of these spectra, instead of using BC and NC individually as in Figures 5 and 6, we fit the full line shape with a two-Gaussian model based on the measured FWHM of BC and NC as was done for the 2.9 μm lines in Banzatti et al. (2017), to test whether there is evidence for both components contributing to the observed water line profile. The analysis of this small sample confirms that water rotational lines at 12.4 μm overall well match the shape of the NC, but it also shows that water lines include weak broad wings from a broader velocity component similar to the BC.

All together, the picture emerging from the kinematics of spectrally resolved water emission observed between 2.9 and 12.4 μm is that water lines are broader at shorter wavelengths in the rovibrational bands and narrower at longer wavelengths in the purely rotational transitions. This suggests that rovibrational lines are excited predominantly (or exclusively) in an inner, hotter region as compared to the rotational lines, a region that may match that of the BC in CO. The rotational lines, instead, are dominated by an emission component that matches the NC in CO, at least down to upper-level energies of $\sim$4000 K as covered in the VISIR and TEXES spectra; lower-energy levels at longer wavelengths covered by JWST-MIRI remain to be spectrally resolved, and might be even narrower by being excited in outer disk regions (see Section 5). The fact that water lines at different wavelengths should have different FWHMs reflecting excitation from a wide range of emitting regions (broader to narrower from higher- to lower-level energies) has been the fundamental expectation of model predictions for some time (e.g., Blevins et al. 2016; Woitke et al. 2016), and this multiwavelength high-resolution data set directly confirms it for the first time. We will combine the picture emerging from line kinematics to that emerging from line excitation in Section 4.4.

4.1.1. Blueshifted Absorption in H_2O Spectra

Two peculiar cases to note in the context of water line profiles and their kinematic structure are those of VW Cha and V1331 Cyg (Figures 5 and 6). The water spectrum observed with VISIR in VW Cha shows a potential narrow absorption line blueshifted from the peak of the emission line (Figure 8). This emission+absorption structure is observed similarly in both water lines that are covered and detected in this object, and the absorption line is much narrower than the telluric lines (Appendix B); we cannot attribute this feature to any artifact possibly present in the VISIR spectra at the time of observation, and we present it here as a potential first detection of a blueshifted absorption feature in mid-infrared water spectra from disks. It should be noted that highly blueshifted [Ne II] emission at -150 and -40 km s^{-1} has been observed in VW Cha in this same VISIR survey (Pascucci et al. 2020), demonstrating the presence of an outflow that could also be linked to the absorption feature in the water lines (although if that is the case, [Ne II] would trace an atomic part of the outflow at higher velocities).

A unified scenario for emission and absorption in the context of an inner disk wind has been proposed to explain blueshifted

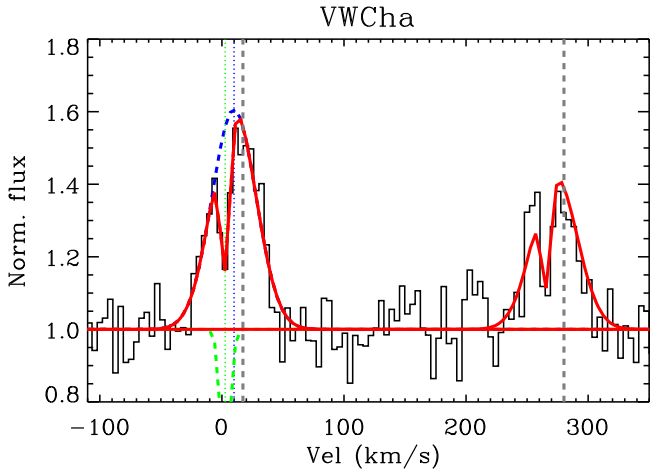

Figure 8. Emission and absorption components in VW Cha, as observed with VISIR in two water lines at 12.3962 and 12.407 μm (with velocity axis centered on the stronger line). Relative to the stellar RV (dashed vertical line near each water transition), the Gaussian component in emission peaks at -7.3 km s^{-1}, and the absorption at -14.5 km s^{-1}. The absorption line width is consistent with being unresolved (10 km s^{-1}).

narrow absorption lines that are observed on top of CO emission lines in other disks (Pontoppidan et al. 2011; Banzatti et al. 2022), conditions that have been found since earlier stages of disk evolution with additional complexity due to envelopes and multiple absorption components (Herczeg et al. 2011). A similar blueshifted absorption is possibly detected in the *M*-band water spectrum of V1331 Cyg (Figure 5), a known source of a large-scale jet and molecular outflow (Mundt & Eislöffel 1998; Wu et al. 2004). In this case, the blueshifted water absorption is very similar to the blueshifted CO NC in its centroid and FWHM. Additional epochs of high-resolution and high-sensitivity observations are required to further investigate these potential absorption components in infrared water spectra.

4.2. H_2O Line Detections and Trends

A second point that we investigate in this work is the excitation of water transitions from different energy levels as a function of stellar and disk properties, addressing questions (1) and (3) from Section 1. Previous work identified the following trends from spectrally unresolved water emission observed at 12–17 μm: (1) water detections are much higher in K and M stars as compared to earlier types (Pontoppidan et al. 2010a) and lower in M-dwarf disks (Pascucci et al. 2013), (2) water detections are lower in disks with inner dust cavities (Salyk et al. 2011b; Banzatti et al. 2017), (3) water line fluxes correlate with stellar luminosity in T Tauri stars (Salyk et al. 2011b) and, more strongly, with their accretion luminosity (Banzatti et al. 2020), (4) water line fluxes anticorrelate with the disk dust radius as spatially resolved with millimeter interferometry (Banzatti et al. 2020). As noted before, the analysis of water spectra is intrinsically a multidimensional problem where multiple star/disk properties affect the observed emission (see, e.g., discussion in Banzatti et al. 2020).

We provide in Figure 9 an overview of these and other trends by considering spectrally resolved water lines at 2.9, 5, and 12.4 μm, and spectrally unresolved water lines at 17 and 30 μm (from Spitzer-IRS), including the *M*-band spectrally resolved CO lines for reference. All of the line flux measurements included in this figure are reported in Appendix C. The line luminosity for each row of plots in the figure is, respectively, as measured in: the low-J $v = 1 - 0$ CO lines (Banzatti et al. 2022), the three water lines around 2.9285 μm (Banzatti et al. 2017), the 5 μm stacked line (Figure 5), the 12.396 μm line (Figure 6), and the few prominent water features around 17.25 and 30.7 μm included in the plots in Appendix A. In this work we do not reanalyze correlations that have already been presented and discussed in previous work, but we find it useful to include the full grid of plots in Figure 9 to combine in one place tracers, samples, and trends that have been previously considered only separately, for future reference. In this section, we briefly describe the general trends and any notable differences between different tracers, and remark that a comprehensive view of this kind will be increasingly valuable in future work to correctly interpret individual spectra and samples from JWST observations within the broader context of the global structure and evolution of molecular gas in inner disks (see guidelines in Section 5.2).

Since CO lines provide the highest detection rates in molecular lines tracing inner disks (e.g., Salyk et al. 2011a; Brown et al. 2013; van der Plas et al. 2015) and a fundamental reference to interpret other molecular tracers, each data point in Figure 9 is classified according to the kinematic shape of its CO line using a line shape parameter $S = \mathrm{FW10\%/FW75\%}$ (the ratio of the line width at 10% and 75% of the peak flux). Lines identified as "triangular" have $S > 2.5$ (with broad wings and a much narrower line center, associated to disk+wind emission) and double-peaked lines have $S < 2.5$ (with typical line profiles associated to purely Keplerian, symmetric disk emission; see more on the definition and discussion of the line shape parameter in Banzatti et al. 2022).

Trends in CO luminosity—For reference to trends observed in water emission, we first describe trends in the CO line luminosity L_{CO}. L_{CO} as measured in this sample shows trends that are sometimes different or even opposite in the two types of lines (top of Figure 9): in particular, in triangular lines, L_{CO} presents a large scatter without an obvious trend as a function of $M_\star$, while in double-peaked lines there is a strong positive correlation above 1 $M_\odot$ (and similarly is observed in L_{acc}). Other notable trends in L_{CO} are with disk inclination, infrared index n_{13-30}, and millimeter dust disk radius R_{disk}; the latter, excluding the weakest objects that are disks with inner cavities, presents an interesting anticorrelation similar to that found in water in Banzatti et al. (2020). The trends observed in L_{CO} are analyzed and discussed in J. Perez Chavez et al. (2023, in preparation).

Trends in 2.9 μm *water luminosity*—The 2.9 μm water sample was biased toward disks around T Tauri stars with moderate to high accretion rates (Banzatti et al. 2017), resulting in perceived high detection rates (∼45%; Table 1). The relatively small sample in this case does not allow to report strong trends, apart from a general agreement with those observed in CO.

Trends in 5 μm *and* 12.4 μm *water luminosity*—The samples at 5 μm and 12.4 μm are larger but provided detection rates of only ∼20%; despite that, some differences from the trends observed in CO emerge clearly. Water detections are exclusively found in objects that have a triangular CO line shape. These objects have in common a moderate accretion luminosity (0.1–1 $L_\odot$), $T_{\mathrm{eff}} < 6000$ K, detection of jets and disk winds, and CO emitting from within the dust sublimation

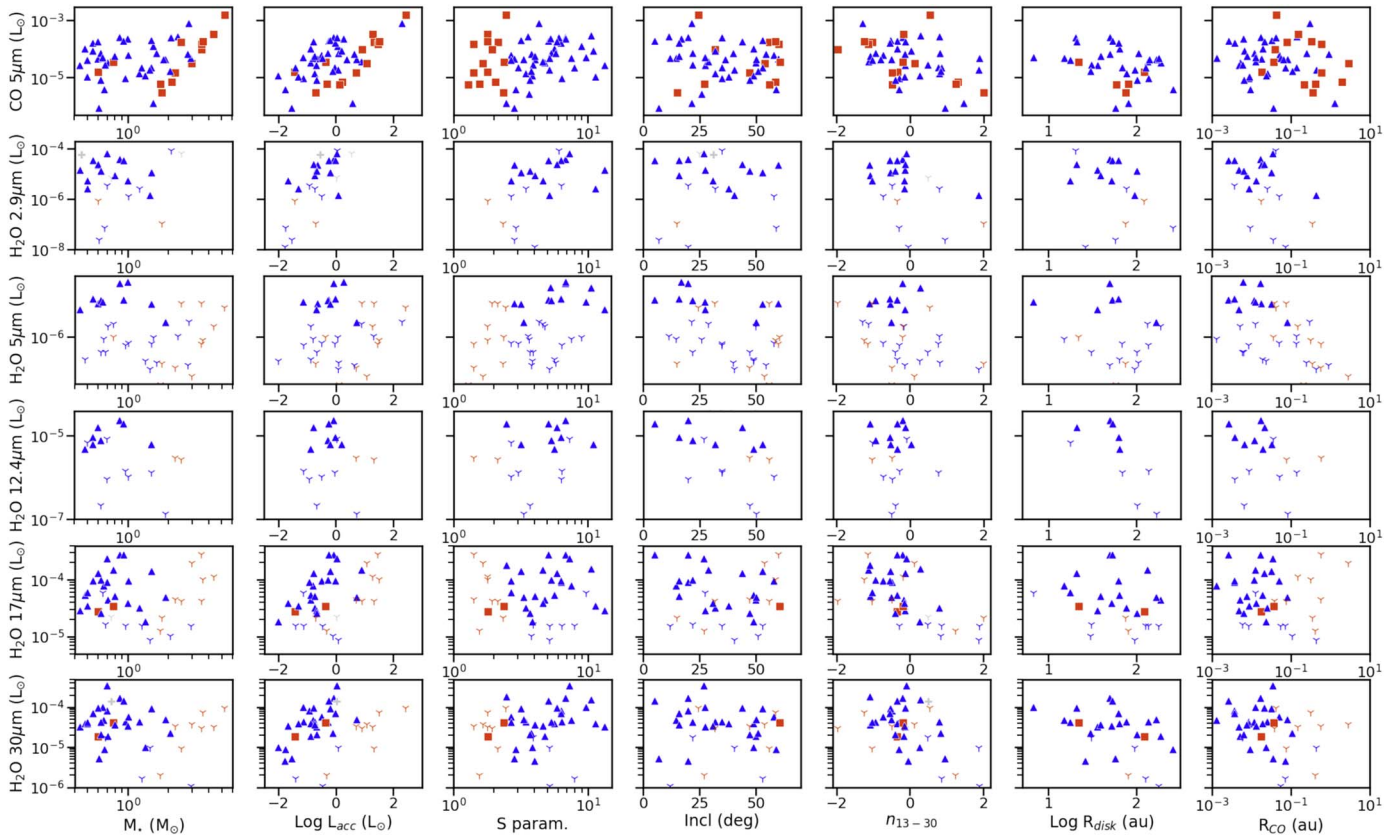

Figure 9. Overview of line luminosity for CO and water lines between 2.9 and 30 μm, as a function of stellar and disk parameters (Section 4.2). Data points are classified according to the kinematic shape of the CO line using a line shape parameter S (Banzatti et al. 2022): "triangular" lines with $S > 2.5$ associated to disk+wind emission (marked with blue triangles), and double-peaked lines with $S < 2.5$ associated to purely Keplerian motion (marked with orange squares). Upper limits are marked with thin symbols. Line flux measurements included in this figure are reported in Appendix C.

radius (see more discussion of triangular lines in Banzatti et al. 2022). The upper limits measured in the 5 μm water lines in some disks around intermediate-mass stars appear in stark contrast with their high CO luminosity, suggesting a different C/O ratio in these disks.

Trends in 17 *and* 30 μm *water luminosity*—Water line detections and luminosity at 17 μm and 30 μm, tracing lower-excitation transitions at 2400–3300 K and 1800 K, respectively, are still predominantly detected in disks with a triangular line shape. An important difference with the higher-excitation water lines at shorter wavelengths is the detection in a Herbig Ae disk (HD 163296, one of the few intermediate-mass stars that has a triangular line shape in CO, which has been associated with an inner disk wind; see Hein Bertelsen et al. 2016b; Banzatti et al. 2022) and in a few disks that have an inner dust cavity (DoAr 44, TW Hya, SR 9, and SU Aur). Detection of water in Spitzer-IRS spectra of these disks was previously reported in Fedele et al. (2012), Salyk et al. (2011b), and Banzatti et al. (2017). These cases demonstrate that rotationally cold water emission can still be observed in some disks with dust cavities and disks around Herbig Ae stars (plots of multiwavelength water spectra are included for reference in Appendix A).

General trends in water luminosity—Across different energy levels (and wavelengths), the water luminosity is in general higher in T Tauri disks than in Herbig disks. The nondetection of water in Herbig disks reflects a true decrease in luminosity and is not simply an S/N issue. In T Tauri disks, the water luminosity increases with accretion luminosity and with line shape parameter S, and decreases with disk inclination, infrared index n_{13-30}, millimeter disk radius $R_{\rm disk}$, and radius of CO emission $R_{\rm CO}$ (estimated from the line width at 10%, as a tracer of the inner emitting radius for warm molecular gas; see Banzatti et al. 2022, for details). The higher detection rates of water in spectral lines with larger S values (e.g., AS 205 N and DR Tau) as observed at high resolution, therefore, are not simply due to the higher line-to-continuum contrast. Broader lines with lower S (e.g., in RNO 90) are more blended with nearby lines (e.g., CO, in M-band spectra) and do require a higher S/N per pixel to be detected, implying that their detection rate will be lower. However, two trends suggest an intrinsically decreasing water (and CO) luminosity due to (1) the S parameter itself, where triangular lines with $S > 5$ have a median luminosity that is ≈5 times higher than triangular lines with $S < 5$, and (2) the viewing angle, where disks with $incl < 25°$ have a median luminosity a few times higher than triangular lines with $incl \approx 30°$–$50°$. Both trends suggest that the geometry of emitting regions as viewed under different inclinations determines the observed properties of molecular spectra (see also Figure 6 in Banzatti et al. 2022).

4.3. Water Rotation Diagrams

The third point we address in this work is the relative excitation of water spectra across different bands and transitions, addressing questions (1) and (3) from Section 1. To do so, we describe the use of rotation diagrams of infrared water emission, which, for the first time, can be analyzed from spectrally resolved emission covering upper-level energies

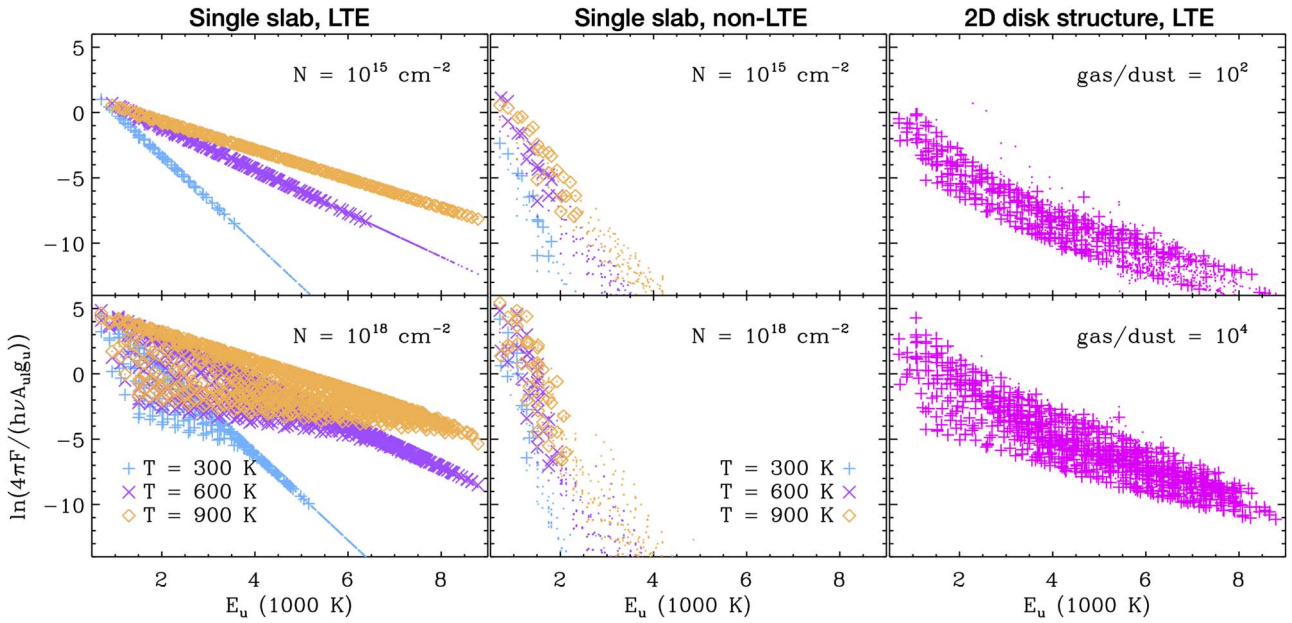

Figure 10. Rotation diagrams of infrared water rotational lines (Section 4.3). Three different models are used to illustrate the effects of different excitation temperatures, line opacity, and LTE/non-LTE excitation: a slab model in LTE (Banzatti et al. 2012), a slab model in non-LTE using RADEX (van der Tak et al. 2007), and a 2D disk structure in LTE using RADLite (Pontoppidan et al. 2009). In each plot and model, larger symbols mark transitions that are stronger than 1% of the strongest line, to simulate a detection threshold; weaker lines are marked with small dots.

between 4000 and 9500 K. The rotation diagram technique has been thoroughly described for space applications in Goldsmith & Langer (1999), but has never been systematically applied to water emission from protoplanetary disks due to the lack of spectrally resolved line fluxes over a broad range in Einstein-A coefficients A_{ul} and in upper-level energies E_u. While this is not necessary with linear molecules in the simplest excitation conditions, covering a large range in E_u and A_{ul} is essential in the case of an asymmetric top polyatomic molecule like water, especially in circumstellar disks where the emission is not optically thin and non-LTE conditions may subthermally excite lines with high A_{ul} (Meijerink et al. 2009; Herczeg et al. 2012; Kamp et al. 2013). Below, we summarize previous explorations by Banzatti (2013) to describe how different conditions (line opacity, LTE/non-LTE excitation) produce distinct features in water rotation diagrams.

4.3.1. LTE Case

Rotation diagrams are defined such that, in conditions of optically thin emission at a single excitation temperature and in LTE, the fluxes from lines at frequency ν observed from an unresolved point source form a straight line as (see Larsson et al. 2002):

$$ln\left(\frac{4\pi F}{h\nu g_u A_{ul}}\right) = ln\left(\frac{N\Omega}{Q(T)}\right) - \frac{E_u}{T}, \quad (1)$$

where F is the integrated line flux, Ω is the solid angle A/d^2 (A is the emitting area of the source, and d is the distance to the source), g_u is the statistical weight of the upper level, $Q(T)$ is the partition function. Throughout this paper, we use E_u in units of kelvin and cgs units for the rotation diagram. The excitation temperature T and the column density N can be easily derived from the slope and intercept of a linear fit using Equation (1). This technique is useful, however, even when the emission becomes optically thick and/or the excitation deviates from LTE. In fact, in these cases the observed molecular line fluxes would produce specific curvatures and/or a large vertical spread in line fluxes in the diagram departing from the linear behavior given by the LTE optically thin case, as described in the following.

The basic properties of rotation diagrams of infrared water emission are displayed in Figure 10 using a single-slab model in LTE (described in Banzatti et al. 2012), with the temperature T and the column density N as free parameters. For this demonstration, we adopt a reference distance of 140 pc and a thermal line broadening of 1 km s^{-1}, and we fix the slab surface area A to a disk with radius 1 au. In the optically thin case ($N = 10^{15}$ cm^{-2}, top left in the figure), water lines form a straight line in the diagram, with slope set by the temperature. It is worth noting that higher T increasingly populate transitions from higher energy levels, as indicated by the larger symbols in the figure. When the column density is increased, instead, line opacities increase and lines spread over the diagram following a specific pattern. When a line gets optically thick ($\tau \gg 1$) it "freezes" on the diagram, i.e., its intensity is only weakly dependent on the column density. This happens first to those lines with large A_{ul} (the low-energy, bottom-left corner of the diagram; see also Figure 11), as the line opacity is proportional to A_{ul}. The optically thin lines, instead, still follow Equation (1) and can rise in the diagram together with N.

Therefore, unlike the case of a linear molecule like CO where a curve is produced, an increase in optical depth for the nonlinear water molecule spreads lines vertically in the diagram. The most optically thin lines (those with the lowest A_{ul} at any given bin in E_u) define the upper edge of the spread, while the most optically thick ones progressively set the middle and lower edge (Figure 11). In these conditions, the vertical spread in the diagram is primarily sensitive to the column density. However, as Figure 11 shows, line intensities are larger at the center of the diagram, indicating that low-sensitivity spectra may only detect part of the full rotation

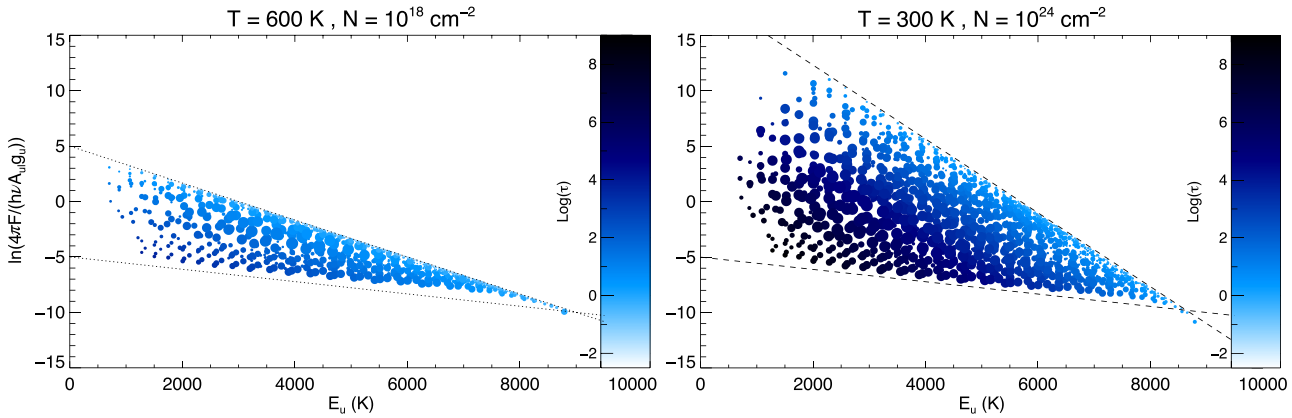

Figure 11. Similar to Figure 10, but including two more properties: the line intensity proportional to dot sizes, and the line opacity τ (proportional to A_{ul}) in blue-color scale. Moderate to high column densities produce optically thick emission and increase the vertical spread of lines in the diagram. The model to the right assumes a very high column density to better illustrate the effect of the spread in line opacities.

diagram (as it typically happens with ground-based instruments; see Section 4.4).

4.3.2. Non-LTE Case

To explore non-LTE excitation, we simulate the emission from a slab of gas using the RADEX code (van der Tak et al. 2007), which accounts for the volume density of the collisional partner H_2. RADEX uses molecular data from the LAMDA database (Schöier et al. 2005) complemented with data from Tennyson et al. (2001), Faure & Josselin (2008), and Dubernet et al. (2009). To better illustrate the effects of non-LTE excitation, we adopt $n(H_2) = 10^6$ cm^{-3}, where water emission is far from being thermalized by collisions (critical densities for infrared water lines are at least $n(H_2) = 10^8$ cm^{-3}; Meijerink et al. 2009). We remark that this is not meant to be an exhaustive exploration but rather a quick reference to the LTE case; a more extensive discussion of non-LTE excitation can be found in Meijerink et al. (2009).

Overall, the rotation diagram shape produced in non-LTE is different from the LTE case (see Figure 10): it displays larger spread or curvature and it produces steeper slopes due to subpopulation of upper levels, which if observed in real data could be interpreted as rotationally cold emission in a "quasi-thermal" behavior (see also Herczeg et al. 2012). It is worth noting in this case that deviations from the LTE case become increasingly apparent at higher energy levels, because critical densities generally increase with E_u.

4.3.3. Disk Structure in LTE

To explore a more realistic disk structure, we adopt the 2D RADLite code (Pontoppidan et al. 2009). RADLite is a raytracer for infrared molecular emission from circumstellar disks, based on the dust temperature and density structure calculated self-consistently using the RADMC code (Dullemond & Dominik 2004). RADLite accounts for dust and gas opacities, and here we set the gas temperature equal to the dust temperature and LTE excitation for simplicity. In modeling the water emission, RADLite takes into account the effects of a snow line set by the temperature and density structure of the disk (Blevins et al. 2016). We set the water abundance to solar oxygen values ($\approx 10^{-4}$ relative to hydrogen) inward of the snow line (where $T > 170$ K), and a low, constant value of 10^{-9} per hydrogen outside of it to simulate freeze-out onto dust grains. For illustration, as a reference model, we assume a 0.01 $M_\odot$ flared disk around a 1 $M_\odot$ star and gas-to-dust ratios (GTDs) of 10^2, to mimic interstellar medium conditions, and as high as 10^4 to mimic dust settling as in Meijerink et al. (2009).

The most distinct feature that can be observed in rotation diagrams of water emission from RADLite, as compared to the slab models, is a curvature due to the contribution of a range in temperature and density from different disk radii (Figure 10, plots to the right). Models also show that the GTD determines the spread of lines in the rotational diagram, by regulating the column of water observable above the dust continuum. Even in this case, the vertical spread in the rotation diagram is linked to the spread in observed line opacities, similarly to slab models, and indicative of the observed water column density. The shape and spread of lines in the rotational diagram of water vapor emission can therefore be useful to generally evaluate the contributions from different effects, provided that the observations cover a large enough range in E_u and A_{ul}.

4.4. Observed Rotation Diagrams and LTE Slab Fits

After briefly describing general properties of the technique in the previous section, we now illustrate in Figure 12 for the first time rotation diagrams of spectrally resolved infrared water emission at energies of 4000–9500 K, for the small sample of disks where the emission is detected in this energy range (see Section 4.1). Previous attempts to retrieve line fluxes over a similarly large range were done by de-blending Spitzer-IRS spectra in Banzatti (2013), but were strongly limited by the low resolution of the data and blending between lines from different levels and molecules. Here, we simply measure and include in Figure 12 the total flux from ~20 lines as observed in Spitzer-IRS spectra to extend the observed rotation diagram down to 1000 K, but we warn the reader that this is done for illustration only and that all of the measured fluxes are blends of multiple transitions. This problem will be solved with JWST-MIRI spectra, as discussed below (Section 5.2).

The largest portion of the observed rotation diagrams is provided by *M*-band spectra, which cover the largest number of water lines from a single high-resolution spectrum (Section 2) and energies between 4000 and 9500 K. In this work, these lines are observed in the iSHELL spectra, which are flux calibrated using Wide-field Infrared Explorer (WISE) W2 photometry at 4.6 μm (Cutri et al. 2021). The high-energy end of these lines overlaps with lines extracted from *L*-band spectra

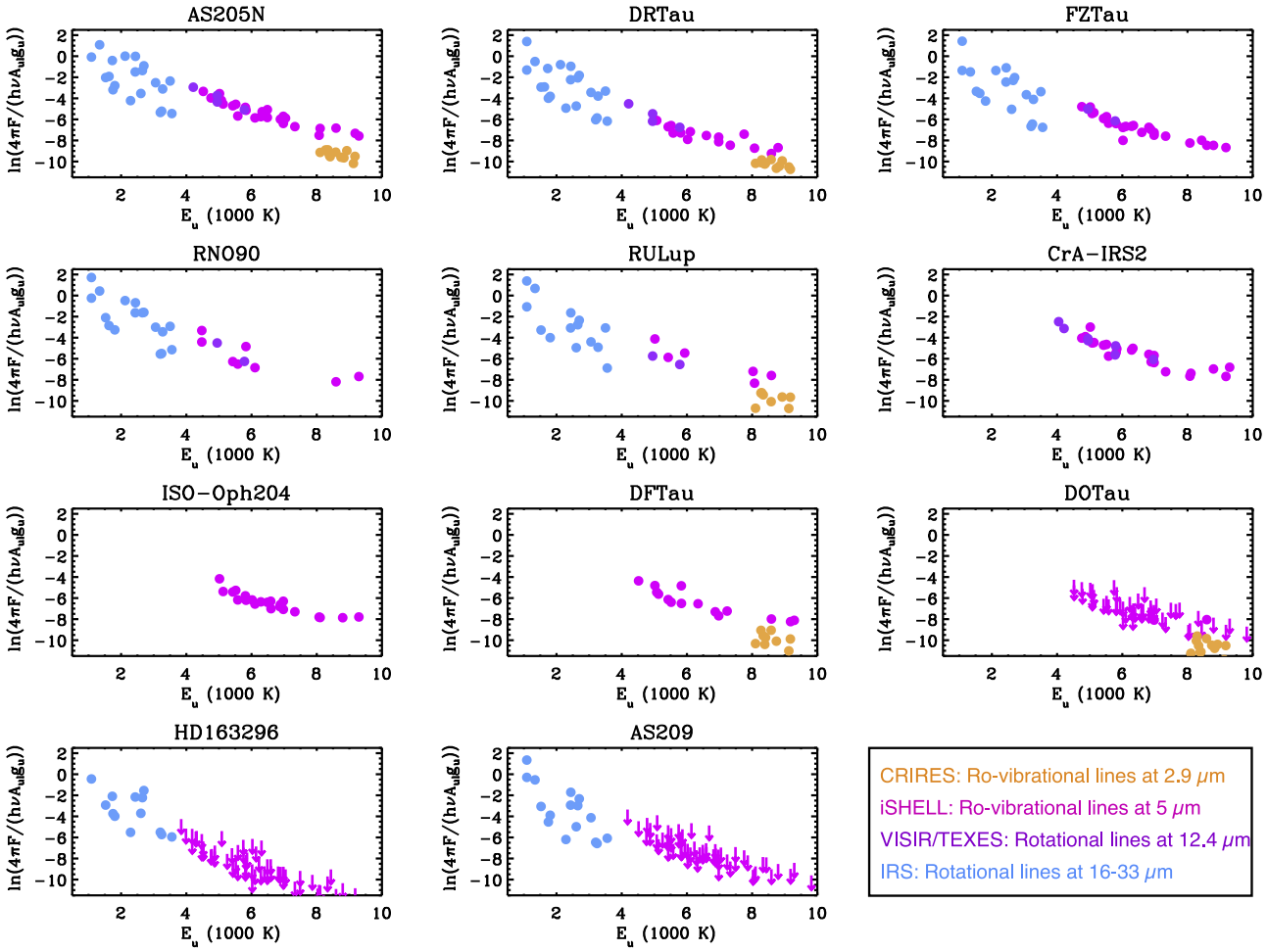

Figure 12. Rotation diagram of water emission as observed at multiple wavelengths in a selection of disks with water detections. Line flux measurements are reported in Appendix C. The last two plots at the bottom are examples of rotationally cold water detected in Spitzer-IRS spectra (see also the multiwavelength plots in Appendix A).

previously observed with CRIRES (flux calibrated using WISE W1 photometry at 3.4 μm), while the lower-energy end overlaps with the rotational lines observed with VISIR and TEXES (flux calibrated using Spitzer-IRS, where available, or WISE W3 photometry at 12 μm). Overall, spectral lines from different instruments overlap well in the rotation diagram of each object apart from the *L*-band lines, which look under-excited as compared to the *M*-band lines in all disks. While real variability and the nonsimultaneous flux calibration may offset the emission as observed with different instruments at different times, the apparent systematic offset between rovibrational bands suggests a difference in their excitation (see Section 5).

Considering line fluxes from different instruments, the observed rotation diagrams show an overall curvature that is reminiscent of what is found from the 2D disk model in Figure 10 as due to emission from a range of temperatures at different disk radii. These curvatures could not be seen before in previous work that only covered <10 lines in a narrow portion of the diagram at 4000–6000 K (Pontoppidan et al. 2010b; Salyk et al. 2019), and are now most evident in the *M*-band spectra alone, as well as in combination with the Spitzer-IRS spectra. In addition to a curvature, lines from the Spitzer-IRS spectra spread vertically as expected in the case of large water column densities (Figure 10). The vertical spread is more visible than in the case of spectra from ground-based instruments, because these have more stringent sensitivity limits and only detect stronger lines close to the upper edge of the rotational spread (Figure 11). By better de-blending line fluxes at mid-infrared wavelengths and detecting weaker lines with lower A_{ul}, the analysis of JWST spectra will reveal the shape and spread in rotation diagrams in higher detail (see Section 5).

4.4.1. LTE Slab Fits

To investigate the excitation of water in different bands and energies, we fit the measured line fluxes with the same LTE slab model adopted above in Section 4.3. The fit is done on the line fluxes directly by simulating spectra with the resolving power and observed line FWHM from each instrument, and minimizing the chi-square between measured and model line fluxes over the same individual spectral window around each line (the flux included within twice the FWHM of each line). The model includes line opacity and accounts for line blending as observed at the resolution of each instrument, rather than assuming optically thin emission to perform a linear regression fit in the rotation diagram.

Table 3 reports the fit results as obtained from spectra at different wavelengths, which are illustrated above in a few examples in Figures 2, 3, and 4. We report results in terms of T and N, which are most sensitive to the measured flux ratios

Table 3
Emission Properties from LTE Slab Model Fits at Different Wavelengths

Object	H_2O 2.9 μm			H_2O 5 μm			H_2O 12.4 μm			CO 5 μm - BC	CO 5 μm − NC
	FWHM (km s^{-1})	T (K)	log N (cm^{-2})	FWHM (km s^{-1})	T (K)	log N (cm^{-2})	FWHM (km s^{-1})	T (K)	log N (cm^{-2})	FWHM (km s^{-1})	FWHM (km s^{-1})
AS 205 N	28	1200	8.2e17	40	1140	3.4e18	23	780	2.0e18	58	16
CrA-IRS 2	⋯	⋯	⋯	45	970	2.5e18	33	790	2.0e18	60	18
DF Tau	(80)	⋯	⋯	100	1880	2.1e18	⋯	⋯	⋯	113	49
DO Tau	(70)	⋯	⋯	(70)	nc	nc	⋯	⋯	⋯	70	19
DR Tau	27	970	1.7e18	22	1160	1.2e18	16	nc	nc	33	12
FZ Tau	⋯	⋯	⋯	40	1060	2.5e18	24	730	6.0e16	51	19
IRAS 04303	⋯	⋯	⋯	⋯	⋯	⋯	100	585	2.3e18	(200)	(90)
ISO-Oph204	⋯	⋯	⋯	40	1160	1.1e18	⋯	⋯	⋯	54	22
RNO 90	⋯	⋯	⋯	(100)	nc	nc	83	(810)	(7.4e18)	110	62
RU Lup	(65)	⋯	⋯	(50)	nc	nc	(56)	nc	nc	77	26
VV CrA S	⋯	⋯	⋯	⋯	⋯	⋯	25	840	2.2e18	76	19
VW Cha	(80)	⋯	⋯	⋯	⋯	⋯	44	695	6.3e17	72	26

Note. Slab models corresponding to the best-fit values reported in this table are shown for a few examples in Figures 2, 3, and 4. "nc": model fit not converged, typically for the scarcity of line flux detections. Values in parentheses have an uncertainty larger than 20%. Typical uncertainties for the best-fit results are of the order of 100 K in T and a factor of a few in N. Measurements of CO line widths are given in the last four columns for reference to water emission properties (see Figure 13) and are obtained from iSHELL spectra, except for VV CrA S and VW Cha that are from CRIRES spectra. The range of CO emitting radii for BC and NC, assuming a purely Keplerian interpretation of the measured FWHM, can be found in Banzatti et al. (2022).

between lines of different energy and Einstein-A coefficients (especially in the moderately optically thick conditions found in the results); in terms of emitting area A, the parameter that most relies on the overall flux calibration, we find similar values of ≈0.1 au^2 for the 2.9 and 5 μm rovibrational lines, and >1 au^2 for the 12.4 and 16–33 μm rotational lines, indicating widely different emitting areas for different transition bands.

The L-band spectrum can be fitted in two disks only, due to the narrow spectral range available, the multiple spectral gaps introduced by telluric and photospheric lines, and severe blending of lines that are typically broad at these wavelengths (see Banzatti et al. 2017). The best-fit excitation temperature is around 1000 K (close to the 900 K previously estimated in a few disks in Mandell et al. 2012) and the column density about 10^{18} cm^{-2}, indicating moderately optically thick emission. Here we measure the full line flux as dominated by a broad component, even though in a few cases there could be a weak contribution from a narrow component in the line peak (see Figure 15 in Banzatti et al. 2017).

The M-band spectrum can be fitted in most disks where water is detected, but does not converge in the case of very broad and very faint emission (DO Tau, RNO 90, RU Lup). The best-fit excitation temperature is around 1100 K, and the column density is about a few 10^{18} cm^{-2}, except for the case of DF Tau where T is possibly as high as 1900 K. The similar results found from the L-band and M-band spectra suggest that the rovibrational bands share a similar excitation, with the stretching mode slightly subthermally excited (which could explain the lower line fluxes in rotation diagrams in Figure 12).

At 12.4 μm, the fit converges only in spectra where at least three lines are detected, while it does not converge in RNO 90 and RU Lup with only two lines. The best-fit excitation temperature is overall around 700–800 K and consistent with what has been found in previous work fitting the 12.4 μm lines (Najita et al. 2018; Salyk et al. 2019), and the column density is about a few 10^{18} cm^{-2}, again indicating moderate optical depth.

At longer wavelengths observed with Spitzer-IRS, temperatures are lower in the range of ≈450 K, as found in previous work (Salyk et al. 2011b). As a comparison test, we have independently measured line fluxes at 16–33 μm from the IRS spectrum of DR Tau and find a best fit with $T = 430$ K and $N = 2.6\text{e}18$ cm^{-2}, a result that is consistent with that found previously in Salyk et al. (2011b).

5. Discussion

5.1. The Picture Emerging from Spectrally Resolved Data

The overall picture emerging from this analysis is summarized in Figure 13, by combining results from Section 4 in terms of line excitation and kinematics as spectrally resolved at multiple wavelengths. LTE slab model fits show that the infrared water spectrum may probe moderately optically thick emission from hotter inner regions exciting the higher energy levels, to colder outer regions populating the lower-energy levels, qualitatively supporting general expectations from previous models (Section 1). The wide range of observable/observed inner disk water column densities (10^{17}–10^{20} cm^{-2}) produced by previous works modeling water spectra from inner disks (Najita et al. 2011; Du & Bergin 2014; Walsh et al. 2015; Agúndez et al. 2018; Woitke et al. 2018) or estimated from spectrally unresolved disk observations (Carr & Najita 2011; Salyk et al. 2011b; Liu et al. 2019) demonstrates that this parameter, and more fundamentally the water vapor abundance as a function of disk radius and disk height (down to the disk midplane), are still, to date, critical unknowns (see discussion in Bosman et al. 2022).

The similar column density found in slab fits to the spectra at different wavelengths (a few times 10^{18} cm^{-2}) across the sample in Table 3 is therefore particularly interesting: recent models that include chemical heating and UV-shielding propose that this is the column density that ends up being probed in the disk surface due to the combination of the most prominent lines becoming optically thick, and the gas temperature steeply falling off at higher densities (Bosman et al. 2022). The results presented above suggest that water spectra across infrared wavelengths may trace gas where the right density for excitation is met at any given disk radius,

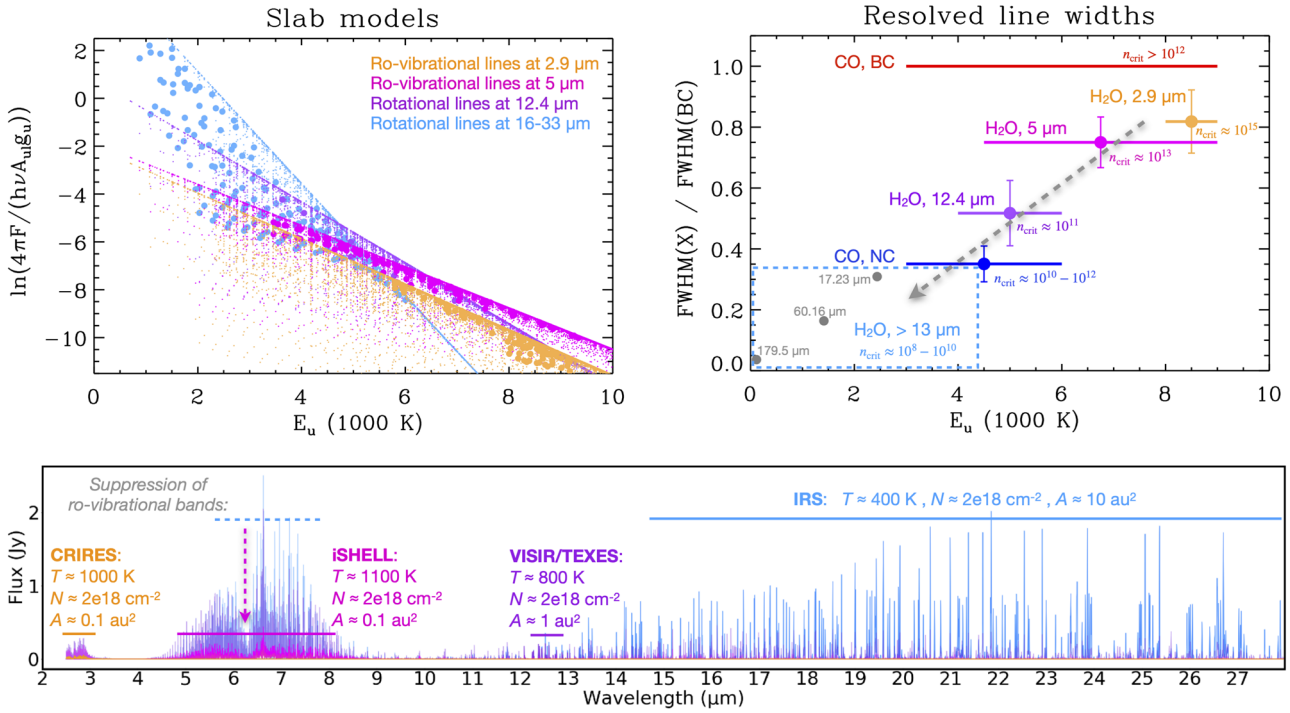

Figure 13. Overview of excitation and kinematics of water emission as spectrally resolved at multiple wavelengths in this work. Top left and bottom: representative LTE slab models from results in Table 3; the overall curvature in the observed rotation diagrams (Figure 12) can be approximated by a series of slab model fits to the different wavelengths covered by different instruments (Section 5.1.1). Non-LTE excitation may cause the suppression of rovibrational bands as compared to slab model fits to the rotational lines (see Section 5.1.2). Top right: observed gradient in line widths as a function of upper-level energy for water and CO (Section 5.1.3); gray data points at 100–2400 K are model predictions for three water lines in RNO 90 using RADLite, from Blevins et al. (2016). Critical densities n_{crit} are reported for reference (see Table 1).

resulting in a similar column density across radii but different excitation temperatures.

5.1.1. A Gradient in Excitation Temperature

The overall curvature observed in rotation diagrams (Figure 12) can be approximated by a series of slab models fitted to the different wavelengths covered by different instruments (i.e., different ranges of energy levels), as reported in Table 3. In the rotation diagram in Figure 13, similarly to Figure 10, we show with small dots each model including all transitions between 2.5 and 33 μm, and then highlight with larger dots the stronger transitions that can be observed in the settings covered by each instrument (the color code follows that of Figure 12). This way, it can be seen that while all models present a large spread of lines due to the moderately large column density (Section 4.3), each instrument ends up observing only a fraction of stronger lines close to the upper edge of the rotational diagram (as observed in Figure 12). The rotational lines at >16 μm are an exception, by tracing a larger part of the vertical spread in the rotation diagram thanks to the wider spectral coverage and higher sensitivity obtained from space.

The same slab models are illustrated in the lower part of Figure 13, marking which spectral range each model is actually sensitive to due to the coverage of each instrument. For guidance, we report representative values for T, N, and A for each model from the fits in Section 4.4. The data demonstrate that no single-slab model can reproduce the whole spectrum, an issue that was noticed early on from fits to the rotational lines in Spitzer spectra (Carr & Najita 2011; Salyk et al. 2011b; Liu et al. 2019) and that this analysis now extends to observations of rovibrational bands at <10 μm.

5.1.2. Non-LTE Vibrational Excitation

Further, it now becomes clear that the vibrational excitation is not in LTE: the fits to rotational lines at >12 μm (from VISIR, TEXES, and Spitzer) strongly overpredict the rovibrational bands at 2.7 μm and 6.5 μm that are observed to be much weaker (using iSHELL and CRIRES). A similar effect is possibly seen also between the two vibrational bands, where the fit to the bending mode overpredicts the emission in the stretching modes. This effect has already been seen in the excitation of M-band CO emission: while an LTE model can reproduce quite well the CO spectrum in both BC and NC in the $v = 1 - 0$ lines, it overpredicts the emission observed from the higher vibrational bands, suggesting subthermal vibrational excitation (see Figure 11 in Banzatti et al. 2022). Water seems to have a similar excitation: slab models can reproduce quite well the emission as observed over different limited spectral ranges and in different bands (Section 4.4), suggesting that the rotational excitation is close to LTE (as expected by models; e.g., Woitke et al. 2018; Bosman et al. 2022), but globally they cannot reproduce the vibrational excitation between the ground state and higher states, implying non-LTE vibrational excitation.

The same conclusion has been reached recently in thermochemical modeling of water in inner disks in Bosman et al. (2022), who proposed that observing weaker emission in the 6.5 μm band as compared to the excitation of the rotational lines would be a signature of non-LTE excitation in low-density gas. This argument now suggests that it is the emitting

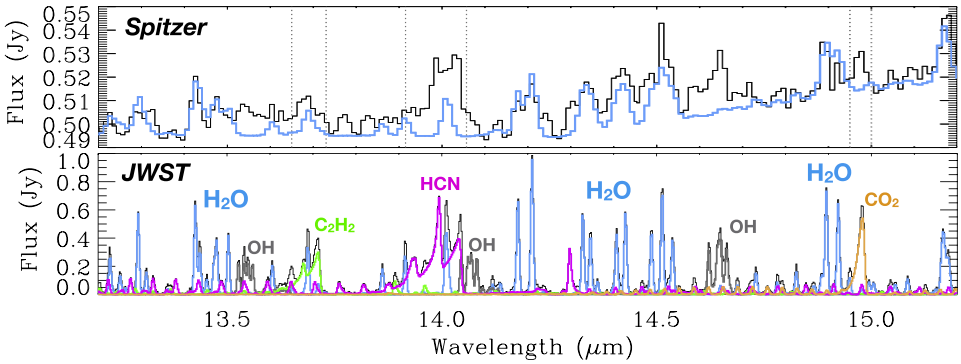

Figure 14. Example of a portion of a Spitzer-IRS spectrum (black, upper plot), compared to an LTE slab model of water emission (in light blue) from Banzatti et al. (2020). The lower plot shows how the same water model would be observed at the resolution of JWST-MIRI, assuming S/N = 100; representative models for other molecules previously identified in Spitzer spectra are included for visualization of the improved de-blending between different lines and molecular spectra.

layer of the rotational lines to be at gas densities lower than the critical density of rovibrational bands ($\approx 10^{13}$ cm^{-3}), because it is the slab model fit to the rotational lines that strongly overpredicts rovibrational emission at <9 μm. This is once again consistent with what is observed in CO: it is the NC (which matches the shape of water rotational lines) to show evident subthermal excitation, while the BC can be matched by an LTE model (Figure 11 in Banzatti et al. 2022).

The higher excitation temperature, larger FWHM, and smaller emitting area found for the rovibrational bands suggest that these must be excited in an inner, denser disk region at higher temperature. The excitation of different energy levels and bands, therefore, globally corresponds to the gradient in critical densities: from 10^{13}–10^{15} cm^{-3} for the water rovibrational bands and the high-J ($E_u = 6000$–9000 K) $v = 1 - 0$ CO lines detected in BC, down to 10^{10}–10^{11} cm^{-3} for the water rotational lines near 12 μm and the CO NC at $E_u = 3000$–6000 K (for CO critical densities, see Thi et al. 2013; Woitke et al. 2016). Water lines at longer wavelengths have lower critical densities of 10^{8}–10^{10} cm^{-3} (Meijerink et al. 2009). These conditions are in accord with detailed laboratory pump-probe experiments that have determined the excitation/de-excitation of vibrational modes in water (and CO) to be orders of magnitude less efficient than the collisional processes that determine the equilibration of the rotational and translational degrees of freedom (Finzi et al. 1977).

5.1.3. A Gradient in FWHM and Emitting Regions

The top right of Figure 13 summarizes the picture emerging from the spectrally resolved line kinematics, using values reported in Table 3. We make this figure in a way to generalize the results to any other disk (see Section 5.2), assuming that the results from the ≈10 disks where water is detected may reflect general properties of Class II disks that do not have an inner dust cavity. For each line tracer X, in Figure 13 we report the median value of the sample distribution of the observed FWHM as normalized to the FWHM of the CO BC in each disk (FWHM(X)/FWHM(BC)). In this way, FWHM differences due to different viewing angles across the sample are removed, putting the figure in the general reference frame of the innermost CO gas observed in any disk (the BC). Each tracer in the figure has a horizontal bar that covers the range in energy levels covered at different wavelengths with the different instruments, and a vertical bar that is the median absolute deviation of the distribution of values across the sample from Table 3. For reference to the H_2O lines, we report also the CO BC (at a y-axis value of 1 by definition, by being normalized to itself in each disk), which is typically detected up to $E_u \approx 9000$ K in this sample, and the CO NC, which instead gets weaker more rapidly than BC at higher energy levels and is more representative of levels up to $E_u < 6000$ K (Banzatti et al. 2022).

As reported above in Section 4.1, the spectrally resolved water rovibrational lines at 2.9 μm and 5 μm have FWHM similar to that of the CO BC, while the water rotational lines at 12.4 μm are instead much narrower and similar to the CO NC, defining the global trend visible in the top right of Figure 13. While the rotational lines at >13 μm remain to be spectrally resolved, we add in the figure the expected FWHM values for three lines (again divided by the FWHM of the BC) from levels down to 100 K as reported in Blevins et al. (2016) using RADLite to model mid- and far-infrared water emission in RNO 90. These previous model predictions, which assumed a radially decreasing temperature profile in a Keplerian disk, show a line FWHM increasing with E_u due to higher-energy lines tracing progressively hotter inner regions, consistent with the global trend emerging from spectrally resolved water emission at higher E_u in this work. In the rest of this section, we discuss some important implications of this global picture for the analysis of spectrally unresolved JWST spectra.

5.2. JWST-MIRI Spectra: Opportunities and Challenges

A total of ∼70 Class II protoplanetary disks are going to be observed with JWST spectrographs in Cycle 1, most of them with MIRI (Rieke et al. 2015) providing $R \approx 1500$–3700 (80–200 km s^{-1}) between 4.9 and 28 μm (Labiano et al. 2021). The wide spectral coverage of MIRI includes the rovibrational bending mode and rotational lines of water vapor emission in disks for the first time at a similar resolution in the two bands (Spitzer-IRS did cover the water bending mode but only with the low-resolution module with $R \approx 60$–120; Sargent et al. 2014). The higher resolving power of MIRI will de-blend many of the emission features previously observed with Spitzer (see example in Figure 14). Fundamental expectations from MIRI spectra are therefore a much improved characterization of the water (and OH) spectrum and its excitation across near- and mid-infrared wavelengths (James et al. 2022), a better characterization of the emission from some organic molecules (although their rovibrational bands near 14 μm will still be severely unresolved; see Figure 14), and the discovery of

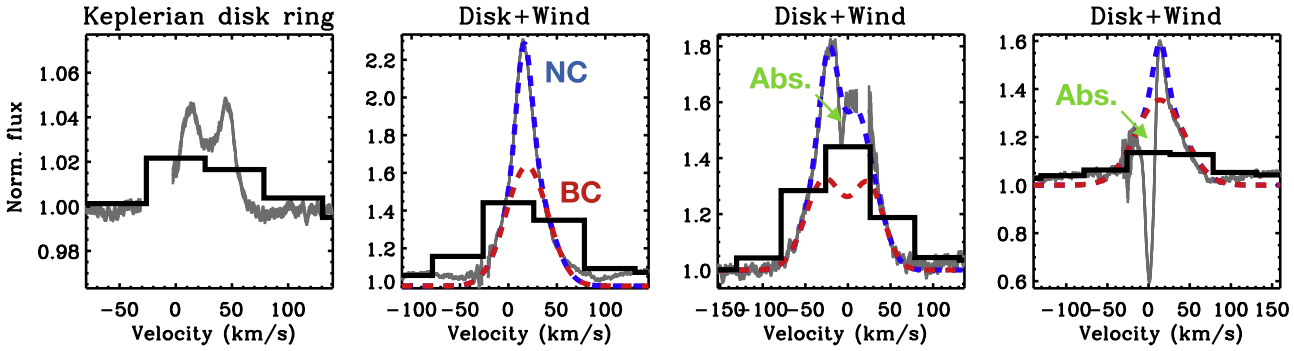

Figure 15. Gallery of representative CO line shapes from *M*-band spectra of inner disks observed with iSHELL (data in gray, from Banzatti et al. 2022, and this work), illustrating the loss of kinematic information and blending of different components when observed at the resolution of MIRI (in black, note how absorption and emission may cancel each other out in MIRI spectra).

features from additional molecules previously unidentified in Spitzer spectra.

MIRI will not provide, instead, measurements of the gas kinematics and the distinction between double-peaked (Keplerian) and triangular line shapes, between BC and NC (where present), and between emission and absorption components observed in inner disks (Figure 15). At most, MIRI is expected to partially resolve the wings of emission lines that are broader than $\approx$100 km s^{-1} (Figure 15). By combining advantages and disadvantages, we describe in the following a number of guidelines for future work to support the analysis of space data and propose how the combination with ground data may be used to obtain a comprehensive understanding of molecular spectra from inner disks.

5.2.1. The Emitting Regions and Excitation of H_2O

From the data and analysis included in this and previous work, it is clear that infrared water spectra observed from inner disks trace a range of emitting regions producing different line widths and different excitation (Figure 13). This picture is naturally expected by disk models (Section 1.1) and provided good fits to rotational lines using slab models that include a distribution of temperatures (Liu et al. 2019). Yet, the absence of spectrally resolved observations, the several uncertainties in the physical and thermal structure of inner disks (both radially and vertically), and the possibility of non-LTE excitation made previous thermochemical modeling of infrared water spectra challenging and degenerate (e.g., Meijerink et al. 2009; Kamp et al. 2013; Antonellini et al. 2015; Woitke et al. 2018; Bosman et al. 2022). Without direct support from spectrally resolved line kinematics, the modeling of MIRI spectra will still have to essentially rely on fitting line fluxes from different E_u and A_{ul} to reconstruct the radial and vertical distribution of water vapor across disk radii. The analysis included in this work identifies some useful guidelines:

1. Rotation diagrams of observed water spectra will reveal large spread and curvature across energy levels (Figures 12 and 13), indicative of optically thick emission (current results suggest a column density of a few $\times 10^{18}$ cm^{-2}) from a range of excitation temperatures ($\approx$300–1100 K); MIRI spectra will be sensitive to detect a larger part of the spread of observed rotation diagrams and better measure the observable column density by detecting weak lines with low A_{ul} (Figure 11).
2. Single-temperature slab models in LTE can be expected to provide good fits to JWST spectra over narrow ranges of E_u and within the same band (e.g., the rovibrational bending mode around 6.5 μm), but the rotational spectrum at >10 μm, which overall spans a large range in E_u from a larger emitting area, will require accounting for gradients in excitation conditions (at least a temperature radial gradient; e.g., Liu et al. 2019).
3. Using the spectrally resolved line shape and FWHM from rovibrational CO spectra as observed from the ground, which are available or currently being obtained for all JWST targets in Cycle 1 (see www.spexodisks.com), Figure 13 can provide general guidance on the expected FWHM for water lines as a function of E_u, which can be used to determine the emitting regions in disks. For a limited number of disks observed from the ground, this can be done by directly using spectrally resolved water emission at multiple wavelengths (Table 3).
4. The rovibrational bands at 2.7 and 6.5 μm show different temperature and non-LTE vibrational excitation as compared to the rotational lines at >10 μm, and trace different disk regions as shown by their different FWHM (Section 4); modeling of JWST spectra will need to account for these differences in excitation conditions.
5. The infrared water spectrum can be expected to first approximation to be rotationally in LTE, but not vibrationally, similarly to what is observed in CO spectra (Section 5.1); detailed analysis of MIRI spectra might reveal more subtle non-LTE effects in the rotational excitation too (Meijerink et al. 2009).
6. Obtaining a good model fit to the observed water spectra will be important for the correct analysis of emission from other molecules too, e.g., the organics at 13–15 μm that are blended with water (Figure 14).

5.2.2. CO- and Water-rich Inner Disk Winds?

The kinematic structure of *M*-band CO lines observed at high resolution from most T Tauri disks can be decomposed into two velocity components, BC and NC, that show very different FWHM and vibrational excitation (Bast et al. 2011; Banzatti & Pontoppidan 2015; Banzatti et al. 2022). Of these components, NC has been associated with a disk wind due to a number of observed properties, most notably the common presence of blueshifted asymmetries (Brown et al. 2013; Banzatti et al. 2022) and an asymmetric spectro-astrometric signal detected in a few disks (Pontoppidan et al. 2011). The similar properties of NC across T Tauri disks, once projection effects at different viewing angles are considered, and the

presence of blueshifted absorption components suggest that the NC may trace a slow molecular inner disk wind in T Tauri disks in general (see discussion in Banzatti et al. 2022).

The similarity between the profile of NC in CO lines and that of water lines at 12.4 μm (Figures 6 and 7) therefore raises the question of whether water may trace the same molecular inner disk wind as CO. MHD disk wind models find that water and CO should be present in a low-velocity molecular region of inner disk winds (e.g., Panoglou et al. 2012; Yvart et al. 2016; Wang et al. 2019), suggesting that the infrared molecular spectra could indeed trace a wind. The narrow absorption tentatively detected in water lines in two disks (Section 4.1.1) may also suggest water-rich outflowing gas, similarly to the absorption observed in CO (Banzatti et al. 2022). The current data set does not show a correspondence between CO absorption and water absorption in lines at $E_u \approx 4000$–6000 K (Figure 6 and Appendix A), but water lines at >13 μm are yet to be spectrally resolved to test whether any absorption may be present at lower E_u. The quality and number of high-resolution water spectra do not allow a definitive answer yet on water, but a few useful guidelines can be formulated for future work to study molecular inner disk winds at infrared wavelengths:

1. Absorption components, where present, will be blended to emission at the resolution of MIRI (Figure 15); MIRI spectra will observe, in these situations, weaker emission lines that will be particularly affected in the case of deep absorption. These situations can be expected to be more frequent at high disk inclinations when the line of sight intercepts gas at or above the disk surface (see Sections 4.6 and 5.3 in Banzatti et al. 2022); high-resolution CO spectra from the ground will support the identification of disks with line absorption, but it is still unclear how much that may affect the water spectra and over which energy levels (Section 4.1.1).
2. In the absence of direct measurements of gas kinematics from spectrally resolved water emission lines in individual disks, models may have to explore the distinction between disk emission and any emission from a wind from the excitation of water and CO spectra, from estimates of their density and temperature. Advancements in models to simulate molecular line profiles from molecular inner disk winds in protoplanetary disks (e.g., Panoglou et al. 2012; Wang et al. 2019; Tabone et al. 2020; Rab et al. 2022) may also provide more guidance in the future.

5.2.3. Measuring H_2O/CO Ratios in Inner Disks

Another fundamental expectation from the analysis of JWST spectra is the possibility to characterize inner disk chemistry and its connections to planet formation. Models expect that the excitation of infrared molecular lines and bands will reflect chemical signatures (e.g., different C/O ratios) as well as dynamical processes (e.g., inner disk oxygen enrichment from icy pebble drift) in individual as well as in ratioed molecular tracers (e.g., Najita et al. 2011; Bosman et al. 2017; Woitke et al. 2018). Some trends possibly related to different C/O ratios due to the drift of icy solids have been measured from water and HCN spectra observed with Spitzer (Najita et al. 2013; Banzatti et al. 2020), but their interpretation is still tentative. A fundamental problem is still how to reliably estimate, using disk models, the column densities from observed spectra that only trace an upper disk layer, and in turn the elemental C/O ratio deeper down in the disk midplane (e.g., Walsh et al. 2015; Woitke et al. 2018; Bosman et al. 2022).

MIRI covers both CO and water in a single spectrum (e.g., Figure 1; see first detection in Yang et al. 2022), avoiding uncertainties in flux calibration and variability that currently affect data obtained from the ground at different times and with different instruments (Section 4). However, MIRI only covers the high-J levels of ^{12}CO lines at >4.9 μm (P25 and up, or $E_u > 4700$ K) and of ^{13}CO (P15 and up, or $E_u > 3500$ K). These ranges of higher J levels lead to large degeneracies in estimates of T and N because they cover a region in the rotation diagram that can be rather flat even when the emission is optically thick, while strong curvatures are only visible at lower J levels (see, e.g., Figure 11 in Banzatti et al. 2022). Measuring H_2O/CO column density ratios in inner disks will therefore be in principle possible from MIRI spectra, but it requires the identification of CO and H_2O lines that trace the same disk region and layer (Figure 13); gaining a more global view of C/O as a function of disk radius will however require one to model a radial density profile in CO and H_2O as observed at multiple wavelengths. Even here, the available spectrally resolved data analyzed in this work provide some guidelines:

1. While rovibrational CO lines, when observed at high resolution, can generally be separated into two discrete components that show different kinematics and excitation (BC and NC), infrared water lines seem to show a more continuous range of line shapes and widths that can only partly be matched by BC and NC or their combination (Section 4.1), making it hard to identify specific lines from different molecules that trace the same disk region.
2. Nonetheless, the rotational water lines with $E_u \approx 4000$ K, close to that of the 12.4 μm lines that almost entirely match the NC line shape (Figure 7), should provide a good match to the NC in CO; by considering the measured FWHM as a function of E_u (Figure 13); these lines could therefore be used to empirically measure H_2O/CO(NC) ratios and their dependence on different stellar and disk properties and their evolution (Figure 9). The question remains of which region in a disk (or wind) layer these specific lines would trace.
3. When observing CO in MIRI spectra, it should be kept in mind that only the high-J lines at $E_u > 4700$ K are covered (Yang et al. 2022), and that these are typically dominated by the BC and are not a good match to the rotational water lines at >10 μm. To measure empirical H_2O/CO ratios from MIRI spectra alone, water lines from the rovibrational band at 6.5 μm and similar $E_u \approx 5000$ K may need to be used.

6. Summary and Conclusions

In this work, we presented the largest data set of spectrally resolved water emission from Class II protoplanetary disks collected to date, as observed with multiple high-resolution ($R \sim$30,000–100,000) spectrographs at infrared wavelengths that are now covered by spectrographs on JWST (from 2.9 μm with NIRSpec to 5 and 12.4 μm with MIRI), for a total of $\approx$160 spectra from a sample of 85 disks (30 of which are targets of JWST programs in Cycle 1). We presented an analysis of the kinematics and excitation of water emission from rovibrational

and rotational lines in different bands observable from the ground, with the goal of obtaining a comprehensive view of the distribution and excitation of water in inner disks.

A correct interpretation of water spectra from disks requires observations across IR wavelengths, supporting the key role that JWST is going to play in this field. This analysis shows that MIRI spectra will observe vertical spread and curvatures in rotation diagrams of water emission, by tracing a range of emitting regions in a moderately optically thick upper disk layer with excitation temperatures of 300–1100 K. We provided in Section 5 a list of guidelines to support the analysis of the large number of disk spectra to be observed with JWST, including how ground-based high-resolution data will be fundamental to provide the missing kinematic information.

The main findings of this work are:

1. rovibrational water lines at 2.9 and 5 μm (E_u of 4500–10,000 K) have larger FWHMs and higher excitation temperatures (1000–1100 K), while rotational lines near 12.4 μm (E_u of 4000–6000 K) have narrower FWHMs and lower excitation temperatures (800 K); LTE slab model fits suggest that a similar column density is observed in all water bands (a few $\times 10^{18}$ cm^{-2}; Section 4.4);
2. the new 5 μm spectra from iSHELL for the first time directly demonstrate that slab model fits to the rotational lines at >10 μm strongly overpredict the rovibrational emission bands at <9 μm; this is interpreted as evidence for non-LTE vibrational excitation, as discussed in Bosman et al. (2022);
3. the picture emerging from combining line kinematics and excitation is in good agreement with the range in critical density for the different bands: (1) an inner, hotter, and denser disk region exciting the rovibrational water bands and the broad CO component, and (2) a progressively cooler disk surface (and low-velocity region in an inner disk wind) exciting the rotational lines and the narrow CO component (with density $<10^{12}$ cm^{-3} so as to subthermally excite the rovibrational lines); the relative contribution of disk versus wind emission across the different radial regions remains to be clarified.

These results are valid for a small sample of $\approx$10 objects where water is detected at high S/N from the ground (Table 3), which is mostly composed of Class II disks with high accretion, outflows, and/or winds (as observed in, e.g., forbidden optical emission lines), and without a large inner dust cavity (as observed with millimeter interferometry). We also remind the reader that the column density estimates obtained from slab models represent only the observed layer (which could be just 1%–10% of the total column density; see, e.g., Bosman et al. 2022), and assume LTE excitation. Water spectra observed with JWST, supported with line kinematics from higher-resolution ground-based observations, will enable a comprehensive characterization of excitation conditions and of the density and distribution of water (and other molecules) in inner disks on a larger population. Analyses of large samples of deblended (or fully spectrally resolved) molecular spectra will be fundamental to study the properties of molecules in inner disks and translate global trends currently observed in line luminosities (Figure 9) into trends in physical and chemical conditions that are evolving in inner disks, to inform models of planet formation and disk dispersal. We therefore invite the community to make use of the large database of infrared spectra available on www.spexodisks.com, with currently $>$1000 spectra from six spectrographs, to support and complement the analysis of spectrally unresolved JWST spectra in the coming years.

This work includes data gathered at the Infrared Telescope Facility, which is operated by the University of Hawaii under contract 80HQTR19D0030 with the National Aeronautics and Space Administration. This work includes observations made with ESO telescopes at the Paranal Observatory under programs 179.C-0151, 093.C-0432, 095.C-0203, 088.C-0666, and 198.C-0104. This work includes observations made with the Spitzer Space Telescope, which is operated by the Jet Propulsion Laboratory, California Institute of Technology under a contract with NASA. This work includes observations obtained at the international Gemini Observatory, a program of NSF's NOIRLab, which is managed by the Association of Universities for Research in Astronomy under a cooperative agreement with the National Science Foundation on behalf of the Gemini Observatory partnership: the National Science Foundation (United States), National Research Council (Canada), Agencia Nacional de Investigación y Desarrollo (Chile), Ministerio de Ciencia, Tecnología e Innovación (Argentina), Ministério da Ciência, Tecnologia, Inovações e Comunicações (Brazil), and Korea Astronomy and Space Science Institute (Republic of Korea). The authors wish to recognize and acknowledge the very significant cultural role and reverence that the summit of Maunakea has always had within the indigenous Hawaiian community. We are grateful to the Hawaiian community to have the opportunity to conduct observations from this mountain.

The authors warmly thank all of the observatory staff that supported observations at the VLT, IRTF, and Gemini telescopes, additional colleagues involved in the VISIR survey (H.U. Käufl, M.F. Sterzik, E. Flaccomio, G. Meeus, R. Alexander, C. Dullemond, S. Steendam), and the anonymous reviewer for suggestions that helped improving this paper. A.B. acknowledges support from NASA/STScI GO grant JWST-GO-01640. G.J.H. is supported by general grant 12173003 from the National Natural Science Foundation of China. A.C. acknowledges funding from the French ANR under contract No. ANR18CE310019 (SPlaSH), and support from the French National Research Agency in the framework of the Investissements d'Avenir program (ANR-15-IDEX-02), through the funding of the "Origin of Life" project of the Grenoble-Alpes University. E.v.D. has been funded by the European Research Council (ERC) under grant 101019751 MOLDISK and the Deutsche Forschungsgemeinschaft (DFG, German Research Foundation) - 325594231, FOR 2634/2.

Facilities: IRTF, VLT, Spitzer.

Software: `mpfit` (Markwardt 2009), `matplotlib` (Hunter 2007), `seaborn` (Waskom 2021).

Appendix A
Multiwavelength Spectral Plots

Figures 16–20 illustrate portions of spectra in disks that have CRIRES, iSHELL, and/or VISIR spectra of infrared water emission, as included in this work. All spectra can be visualized interactively on www.spexodisks.com.

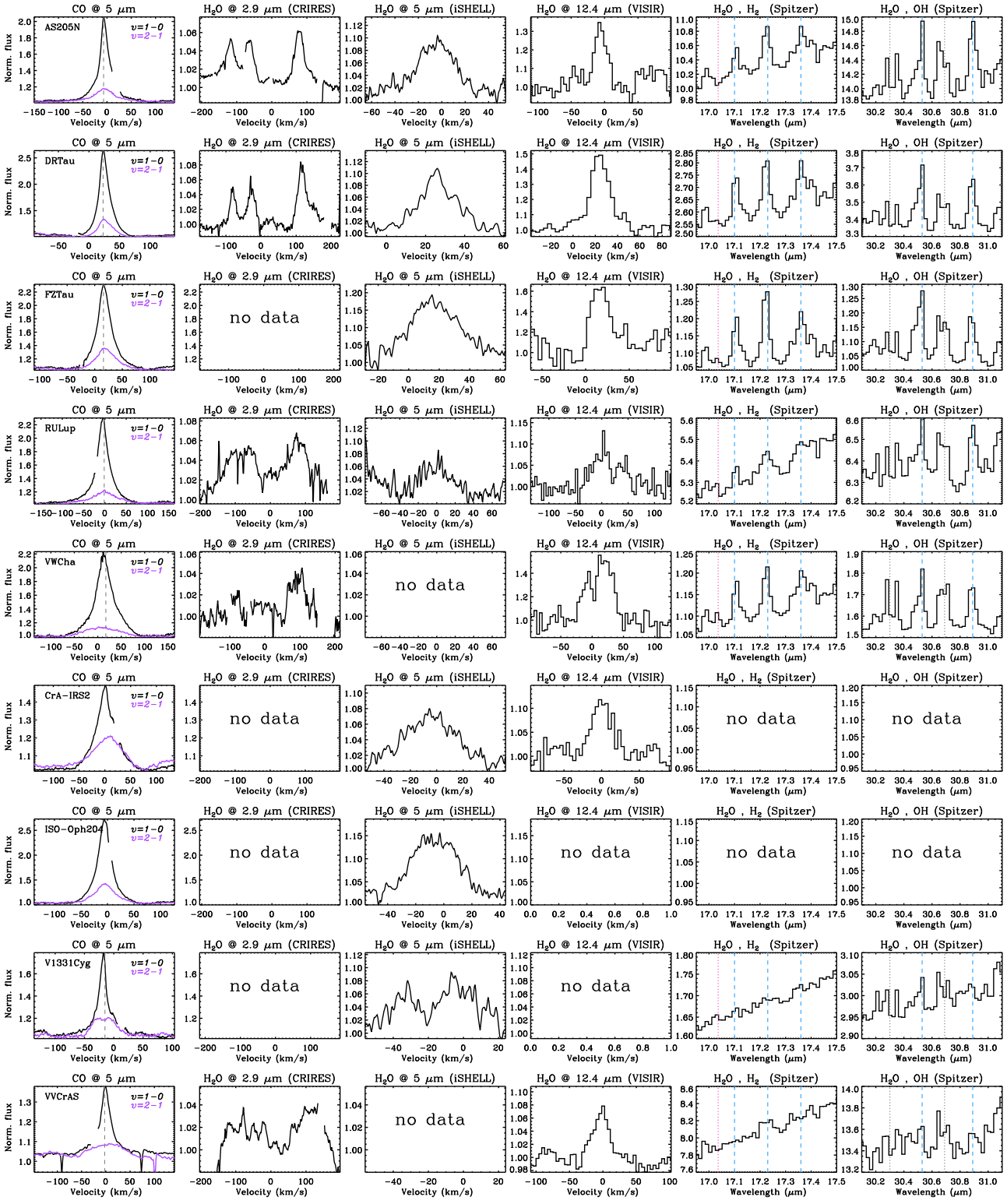

Figure 16. Multiwavelength infrared spectra included in this work. The stellar RV is showed with a dashed line on top of CO lines, where available. High-resolution spectral lines are shown in velocity space and continuum-normalized (the *L*-band lines are shown in reference to 2.9283 μm); those from Spitzer spectra are shown in wavelength and in calibrated flux units of janskys. H_2O emission is marked with dashed lines while H_2 and OH emission are marked with dotted lines in the Spitzer spectra.

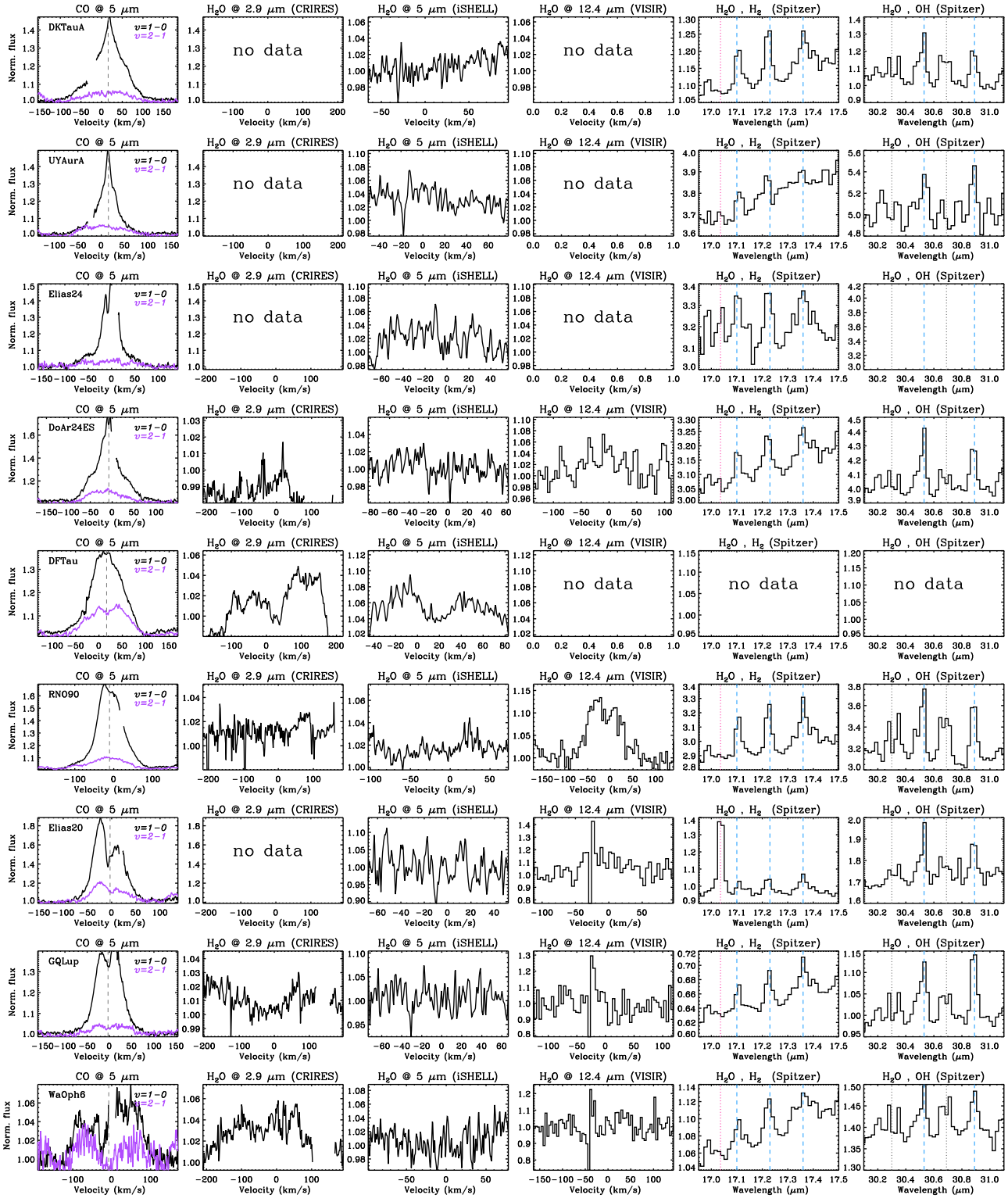

Figure 17. Same as Figure 16, for additional disks.

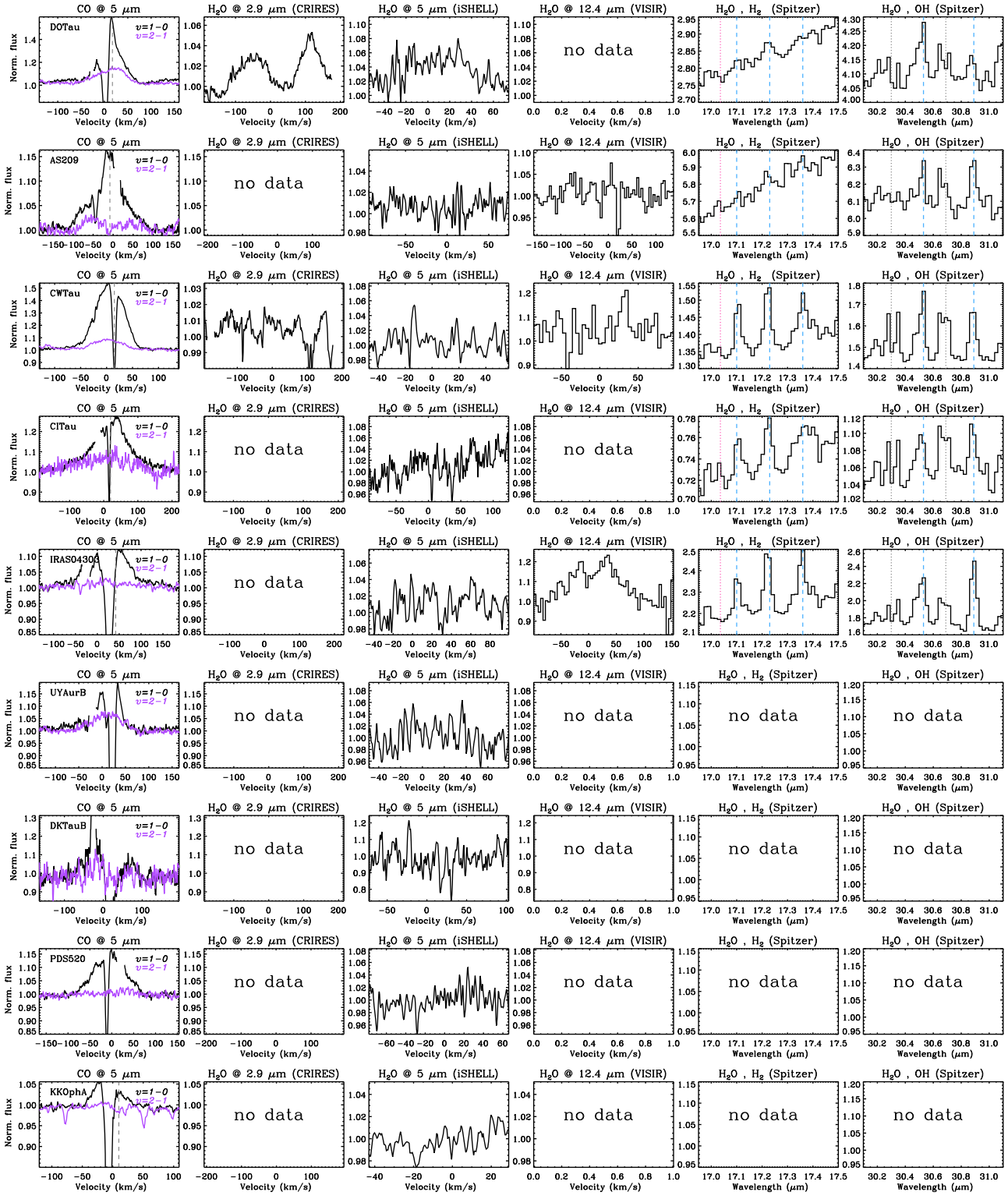

Figure 18. Same as Figure 16, for disks with absorption in CO lines.

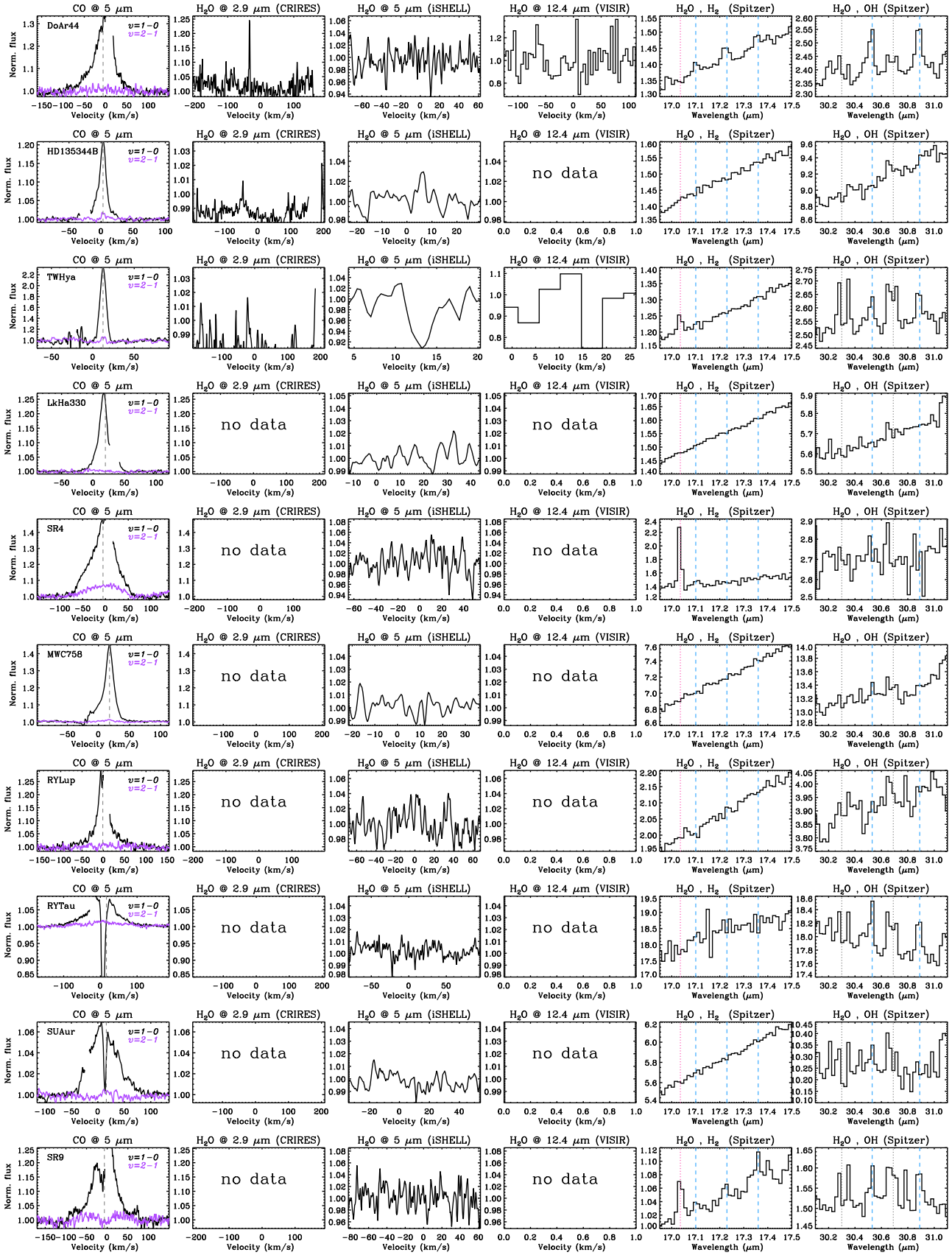

Figure 19. Same as Figure 16, for disks with inner dust cavities.

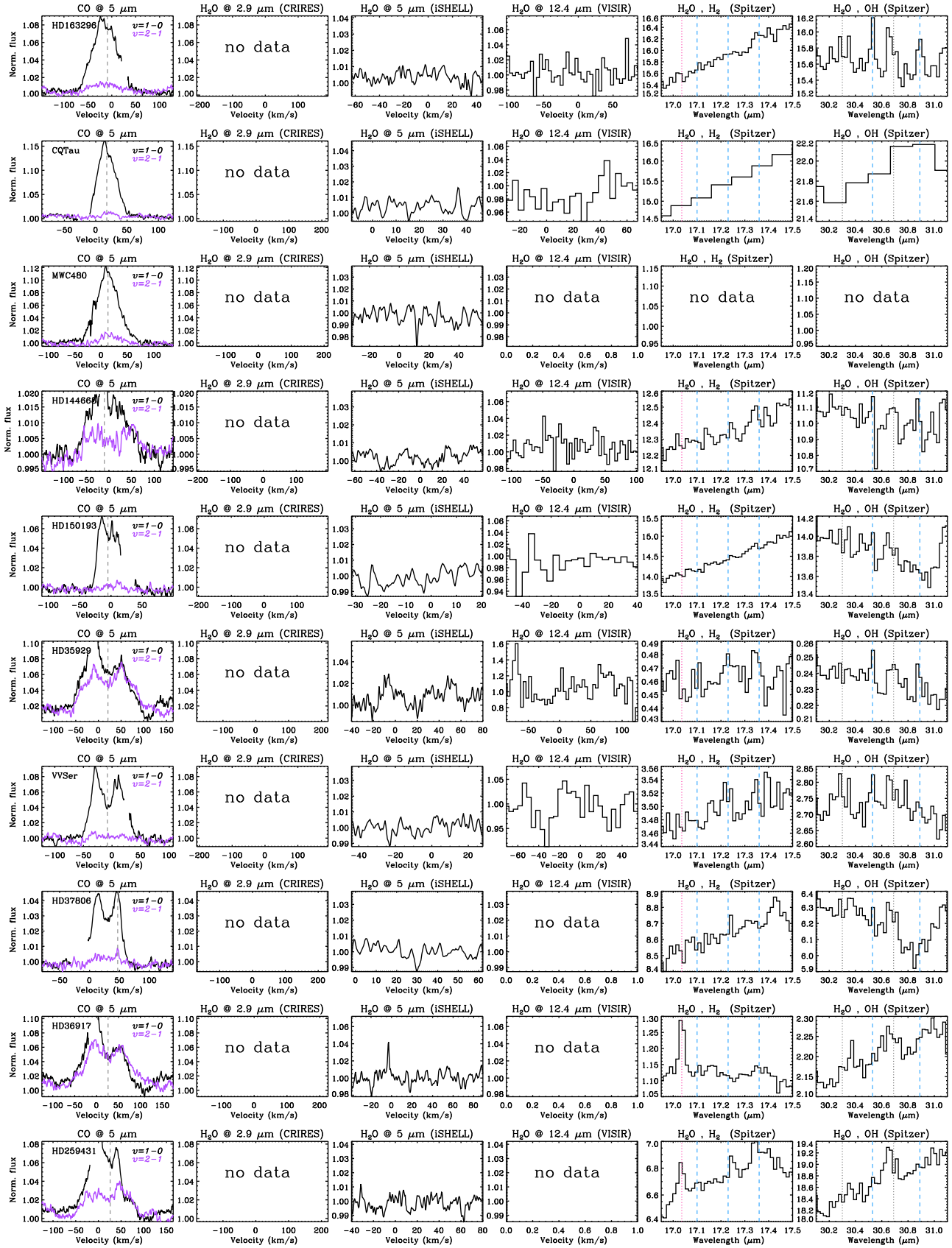

Figure 20. Same as Figure 16, for selected disks around Herbig Ae/Be stars.

Appendix B
A Survey of Mid-infrared Water Spectra with VLT-VISIR

B.1. Data Reduction

With VISIR in echelle mode, the telescope chops off the slit due to the short slit of 4.″1; the nod B positions are therefore used only for background subtraction. Mechanical oscillations of the grating between sequential chops and nods, and sometimes a difficult guiding on weak sources, introduce small shifts (between fractions of a pixel to a few pixels) in both the spatial and spectral directions on the detector. These are corrected by cross-correlation of the position of one echelle order (for the spatial direction) and telluric lines (for the spectral direction), during combination of individual chops and nods. This procedure ensures the correct combination of the point-spread function (PSF) as observed in different nods, and avoids producing an artificial PSF broadening and residuals from the shift of telluric lines. A similar procedure for the spectral direction was previously implemented for VISIR 1 data (Carmona et al. 2008; Banzatti et al. 2014).

Observing *N*-band water spectra from the ground is very challenging due the variability of Earth's atmospheric conditions, especially in the precipitable water vapor (PWV). Apart from exceptional conditions, the sky typically changes significantly between sequential nods and causes residuals from variable telluric lines in the spectra. In this VISIR survey, we carefully monitored the observing conditions nod by nod, and reject individual nods where the sky varied by more than 5σ from the mean sky variation in each observing block. Any remaining sky residuals were removed by averaging the signal over 10–15 pixels at the two sides of the PSF pixel by pixel in the spectral direction, fitting this average with a Savitzky-Golay polynomial smoothing filter, and then subtracting the fit from the PSF before extracting the 1D spectrum. We extensively tested this correction, which in previous work was performed using a simple median subtraction (Pontoppidan et al. 2010b; Banzatti et al. 2014), and found that it gives the best results in removing telluric residuals while minimizing noise addition to the spectral PSF. The 1D spectrum is then extracted using optimal extraction.

After the detector upgrade in 2016, strong high-frequency fringing was found to affect VISIR high-resolution spectra. In connection to that, the sensitivity was also found to be a factor ≈10 lower (Figure 21). In 2017 April, the entrance window of VISIR was replaced to solve this issue. This replacement removed completely the high-frequency fringing in the echelle mode, and suppressed it in the long-slit mode; however, the low-frequency fringing that was affecting VISIR 1 was still present in all modes (see, e.g., Figure 22). Since VISIR observations do not include flats, but fringing was found to not be stable enough to be removed simply by division with the standard, we fitted and removed fringes in each spectrum after extraction of the 1D spectrum and prior to telluric correction. Some fringe residuals remained when fringes varied between a science target spectrum and its telluric standard spectrum and in the spectra of binary systems, where the two components were observed in a different position on the detector as compared to the telluric standard.

Telluric correction of the extracted 1D spectra was performed using observations of several bright asteroids and a few bright stars (Alpha Cen, Alpha Car, Alpha CMa = Sirius, Theta Sco = HR6553). Telluric observations were interspersed during science observations in order to ensure a good match (difference <0.1) in airmass and PWV with the science targets. This was achieved in most but not all cases. Differences in both airmass and PWV between science targets and telluric standards are compensated during reduction using telluric water and CO_2 lines. We have tested using the airmass and PWV values recorded in fits headers, but these average values do not fully capture real differences and variability happening during observations. We therefore scaled telluric water lines until they matched those observed in the science targets to find the best PWV correction, and do the same with a CO_2 line to find the best airmass correction. These correction factors were applied to the telluric spectra as an exponential correction of the form $f_{\rm corr} = f_{\rm obs}^{(A_{\rm science}/A_{\rm telluric})}$ as in previous work (Pontoppidan et al. 2010b; Banzatti et al. 2014). The science and telluric spectra were then normalized to their continua, aligned by cross-correlation of telluric lines, and then divided after applying the airmass and PWV correction to the telluric spectrum.

Wavelength calibration of individual spectra was done by cross-correlation in each setting with an atmospheric model set on Paranal conditions (same model as above in Section 1.1). We fine-tuned the wavelength solution on low-PWV spectra that allowed us to use all of the observed telluric lines out to the detector edges (Figure 22), and then we applied that solution to all other spectra after shifting it by cross-correlation of sky lines in each spectrum.

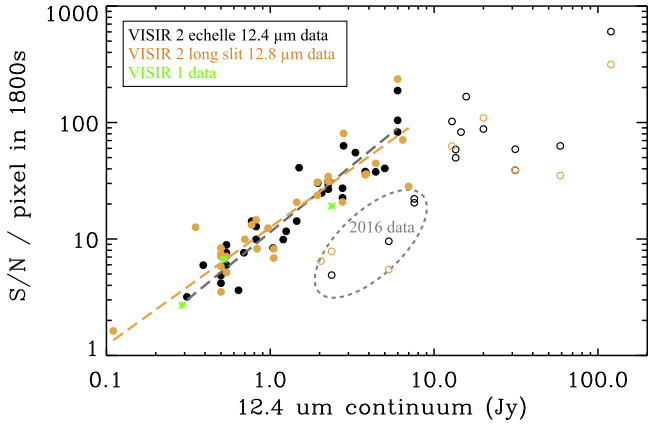

Figure 21. VISIR 2 sensitivity estimated from this survey, as compared to previous data from VISIR 1 (Pascucci & Sterzik 2009; Banzatti et al. 2014). Linear fits to the echelle and long-slit modes are shown with dashed lines. A lower sensitivity is recorded in 2016 after the detector upgrade but before the entrance window was replaced in 2017, as well as in brighter sources.

B.2. VISIR 2 Performance

We measured the spectral resolution of VISIR from unresolved O_3 lines detected in telluric absorption spectra. We used several asteroid observations obtained during the survey and consistently measure an FWHM of $10\,{\rm km\,s^{-1}}$ (corresponding to $R \sim 30{,}000$) in four O_3 lines detected in the 12.84 μm setting. In the other two settings, O_3 lines are much weaker and possibly detected only in a few spectra; these measurements are less consistent and provide FWHMs in the range 5–$13.6\,{\rm km\,s^{-1}}$, suggesting a similar resolution of R ≈30,000 also in echelle mode at 12.2–12.5 μm.

In terms of sensitivity, we find that VISIR 2 observations in the echelle and long-slit settings utilized here delivered a

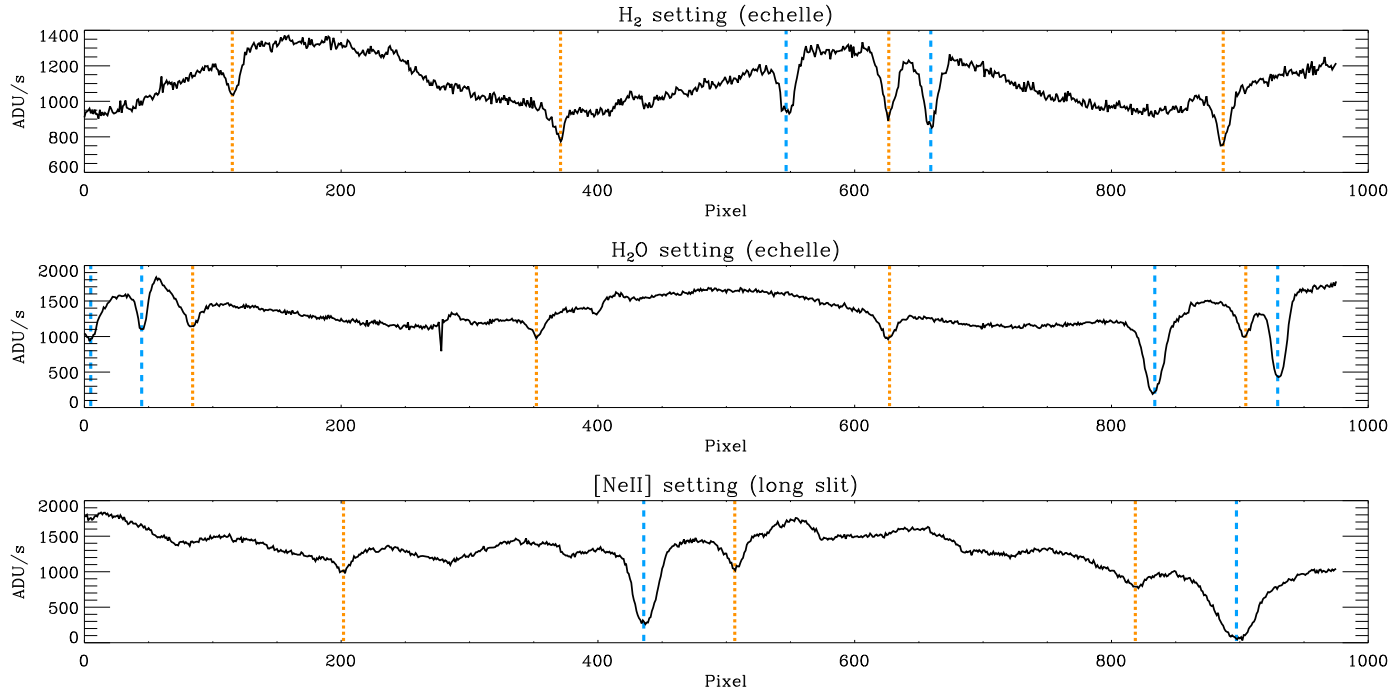

Figure 22. Spectral settings covered in the VISIR survey, shown as extracted from the combined 2D spectra (but before any correction/calibration is applied). The target is CrA-IRS2, which is one of the four targets observed in all three settings. Telluric water absorption is marked with dashed lines, and telluric CO_2 absorption is marked with dotted lines. The echelle settings are affected by lower-frequency fringes, the long-slit setting by higher-frequency fringes.

similar S/N per pixel (Figure 21). Using as reference spectra of DR Tau, *T* Cha, and Sz 73 taken in 2008–2012 (Pascucci & Sterzik 2009; Banzatti et al. 2014), the new sensitivity is ≈60% higher than VISIR 1 observations, after the different pixel sampling has been accounted for (VISIR 2 has a pixel/wavelength ratio larger by 60% than VISIR 1).

Appendix C
Sample and Line Flux Measurements

Table 4 reports the full sample of 85 disks included in this work based on the available high-resolution spectra of infrared water emission. Figure 23 visualizes the sample and settings from the VISIR survey in a Venn diagram. Line fluxes are measured from the CRIRES, iSHELL, and VISIR spectra as available from the different surveys (Section 2) and as explained in Section 4.2. Line fluxes are measured from continuum-normalized spectra because absolute flux calibration of high-resolution infrared spectra from the ground is typically uncertain due to flux losses through narrow slits, which may vary from night to night even for the same instrument due to variable sky conditions. The continuum-normalized line fluxes F_{cn} are turned into the absolute line luminosity shown in Figure 9 using the measured distance and continuum fluxes F_c, as $L = 4\pi\ \mathrm{dist}^2 F_{cn} \times F_c$. As continuum flux F_c, we take the W1 and W2 fluxes from WISE for the 2.9 and 5 μm water lines, and the continuum flux as measured at 12.3 μm from Spitzer-IRS spectra for the 12.4 μm water line. Table 5 reports line flux measurements for transitions covered in the *M*-band iSHELL spectra in four disks that have the largest number of detections. Line flux measurements for the entire iSHELL survey are available upon request to the author.

We report here the SIMBAD name of some objects, for easier identification: CrA-IRS 2 is CHL*T* 1 (2MASS J19014156-3658312), EC 82 is HBC 672 (2MASS J18295688+0114463), Elias 20 and 24 are Elia 2-20 and 2-24, IRAS 04303 is IRAS 04303+2240 (2MASS J04331907+2246342), IRS 48 is IRAS 16245-2423 (2MASS J16273718-2430350), ISO-Oph 204 is 2MASS J16315211-2456156, SR 21 is Elia 2-30, SR 9 is Elia 2-34, and SR 4 is Elia 2-13.

Sample properties used in this work have been collected and reported in Banzatti et al. (2022) for most of the sample. We include here references used in that paper, which are also used for the rest of the sample included in this work: distances are from Bailer-Jones et al. (2018); stellar and accretion properties are from Guzmán-Díaz et al. (2021), Wichittanakom et al. (2020), Herczeg & Hillenbrand (2014), Salyk et al. (2013), Andrews et al. (2018), Fang et al. (2018), and Simon et al. (2016); the infrared index n_{13-30} is measured from Spitzer-IRS spectra as in Banzatti et al. (2020); WISE fluxes are taken from the AllWISE Data Release (Cutri et al. 2021); references for the stellar RV, the disk inclination, and the millimeter dust disk radius R_{disk} are: Alecian et al. (2013), Dunkin et al. (1997), Fang et al. (2018), Banzatti et al. (2019), Liu et al. (2011), van der Marel et al. (2016), Wölfer et al. (2021), Hartmann et al. (1986), Sullivan et al. (2019b), Acke et al. (2008), Brittain et al. (2007), Long et al. (2018), Long et al. (2021), Huang et al. (2018), Kurtovic et al. (2018), Labdon et al. (2019), Pinilla et al. (2018), Tripathi et al. (2017), Ubeira Gabellini et al. (2019), Pontoppidan et al. (2011), and Brown et al. (2012).

Table 4
Sample and Line Flux Measurements

			2.9 μm			5 μm					12.4 μm		
Object	Dist	S	F_c	F_{cn}	err	F_c	F_{cn}	err	F_{cn}(CO)	err(CO)	F_c	F_{cn}	err
51Oph	125.	⋯	11.2	⋯	⋯	35.7	⋯	⋯	⋯	⋯	⋯	−3.02e-16	5.66e-17
AATau	137.	1.8	0.3	4.41e-15	4.41e-15	0.3	⋯	⋯	8.10e-14	5.99e-16	0.3	⋯	⋯
ABAur	155.	3.6	14.8	⋯	⋯	36.7	3.73e-17	2.31e-16	9.69e-15	1.53e-17	⋯	⋯	⋯
AS205N	127.	7.0	4.4	1.67e-14	6.18e-15	6.8	8.73e-15	1.12e-16	7.31e-14	2.69e-16	7.2	6.35e-15	6.25e-16
AS209	121.	6.4	0.8	⋯	⋯	0.8	1.58e-15	3.46e-15	2.56e-14	3.31e-16	3.4	9.06e-16	1.16e-15
CITau	158.	4.8	0.6	⋯	⋯	0.7	3.77e-15	9.91e-15	6.38e-14	6.44e-16	0.5	⋯	⋯
CQTau	149.	9.2	2.3	⋯	⋯	2.9	3.21e-16	6.20e-16	6.81e-15	8.39e-17	4.9	3.85e-16	9.74e-16
CrA-IRS2	150.	6.9	2.7	⋯	⋯	6.5	7.17e-15	9.23e-17	4.91e-14	2.04e-16	⋯	2.65e-15	4.10e-16
CWTau	132.	2.7	1.5	1.56e-15	1.56e-15	1.8	6.95e-16	3.73e-15	6.29e-14	2.09e-16	1.2	1.55e-15	6.51e-15
DFTau	125.	2.9	1.2	3.81e-14	4.95e-15	1.4	1.24e-14	1.90e-16	6.70e-14	1.87e-16	⋯	⋯	⋯
DKTauA	128.	7.6	1.1	⋯	⋯	1.3	1.32e-15	4.41e-15	7.27e-14	4.07e-16	⋯	⋯	⋯
DKTauB	128.	15.1	⋯	⋯	⋯	⋯	−3.44e-16	2.86e-14	−2.52e-15	3.08e-14	⋯	⋯	⋯
DoAr24EN	137.	⋯	⋯	⋯	⋯	⋯	⋯	⋯	⋯	⋯	⋯	−9.42e-16	1.10e-15
DoAr24ES	137.	6.4	⋯	⋯	⋯	⋯	8.12e-16	4.34e-15	9.60e-14	4.12e-16	2.6	5.74e-16	1.05e-15
DoAr44	145.	3.5	0.6	6.26e-15	1.66e-14	0.6	5.66e-18	5.72e-15	3.69e-14	7.91e-16	0.6	⋯	⋯
DOTau	139.	13.5	0.9	2.60e-14	2.09e-15	1.2	8.17e-15	2.74e-16	3.80e-14	4.76e-16	2.0	⋯	⋯
DRTau	195.	5.1	1.4	1.98e-14	2.98e-15	1.9	4.65e-15	1.01e-16	8.26e-14	1.38e-16	1.9	8.43e-15	4.36e-16
EC82	399.	⋯	⋯	⋯	⋯	⋯	⋯	⋯	⋯	⋯	1.5	−2.20e-16	4.90e-15
Elias20	138.	5.6	1.0	⋯	⋯	1.6	2.50e-16	1.08e-14	1.08e-13	6.04e-16	1.0	8.27e-15	7.24e-15
Elias24	136.	4.6	0.7	⋯	⋯	1.3	3.03e-15	5.00e-15	4.88e-14	6.01e-16	2.8	⋯	⋯
EXLup	157.	11.4	0.3	1.16e-14	5.47e-16	0.3	⋯	⋯	4.48e-14	5.07e-16	⋯	3.85e-15	3.08e-14
FNTau	131.	4.0	0.3	7.71e-17	1.54e-16	0.3	⋯	⋯	1.05e-14	3.28e-16	0.7	⋯	⋯
FZTau	130.	5.5	1.1	⋯	⋯	1.3	1.45e-14	1.87e-16	1.03e-13	3.49e-16	1.0	1.43e-14	1.02e-15
GQLup	151.	2.4	1.1	⋯	⋯	1.0	1.32e-15	8.90e-15	4.68e-14	1.18e-16	0.5	−9.79e-16	5.34e-15
HD100546	108.	⋯	6.4	⋯	⋯	7.1	⋯	⋯	⋯	⋯	⋯	1.70e-16	1.06e-15
HD101412	410.	⋯	1.1	⋯	⋯	1.7	⋯	⋯	⋯	⋯	2.4	6.08e-16	2.79e-15
HD135344B	134.	5.2	3.2	7.67e-16	3.03e-16	3.5	6.28e-17	1.12e-15	9.21e-15	1.95e-16	0.9	⋯	⋯
HD141569	111.	2.0	1.2	⋯	⋯	0.6	7.34e-17	1.13e-15	2.86e-14	2.69e-16	⋯	⋯	⋯
HD142666	146.	1.3	2.5	⋯	⋯	3.0	2.35e-17	4.98e-16	2.86e-15	1.22e-16	⋯	⋯	⋯
HD143006	166.	1.6	1.4	⋯	⋯	1.4	−1.34e-18	7.55e-16	4.77e-15	2.12e-16	0.7	⋯	⋯
HD144432S	677.	2.8	⋯	⋯	⋯	⋯	⋯	⋯	1.14e-14	1.57e-16	⋯	−2.73e-16	1.08e-15
HD144668	160.	2.1	32.5	⋯	⋯	61.7	1.69e-16	6.36e-16	3.57e-15	7.82e-17	12.0	2.76e-16	1.16e-15
HD150193	150.	1.4	5.1	⋯	⋯	6.5	3.02e-17	5.18e-16	3.34e-15	1.24e-16	10.8	3.86e-16	4.40e-16
HD163296	101.	3.3	9.8	⋯	⋯	11.6	6.83e-16	4.32e-17	1.17e-14	8.68e-17	11.5	3.60e-17	7.95e-16
HD169142	114.	2.5	1.0	⋯	⋯	0.9	3.99e-18	6.69e-16	3.30e-15	8.01e-17	⋯	⋯	⋯
HD179218	258.	1.7	3.6	⋯	⋯	4.8	7.92e-18	2.25e-16	3.13e-15	1.78e-17	15.6	⋯	⋯
HD190073	872.	4.3	4.0	⋯	⋯	5.6	1.93e-17	1.23e-16	5.80e-15	1.28e-17	5.2	⋯	⋯
HD259431	640.	2.4	5.1	⋯	⋯	9.6	5.25e-17	1.09e-15	1.29e-14	6.29e-17	6.2	⋯	⋯
HD35929	377.	1.9	1.1	⋯	⋯	1.1	1.72e-15	1.79e-15	1.96e-14	2.35e-16	0.6	−3.32e-15	7.06e-15
HD36917	445.	1.8	2.2	⋯	⋯	2.7	1.14e-16	1.76e-15	1.91e-14	9.91e-17	1.2	⋯	⋯
HD37806	397.	1.4	4.5	⋯	⋯	6.7	1.92e-17	5.75e-16	4.56e-15	8.50e-17	8.0	⋯	⋯
HD97048	184.	⋯	5.0	⋯	⋯	2.8	⋯	⋯	⋯	⋯	⋯	3.48e-16	1.17e-14
HTLupA	154.	5.3	1.5	⋯	⋯	1.6	⋯	⋯	2.22e-14	1.45e-16	⋯	⋯	⋯
IMLup	158.	2.9	0.5	1.80e-16	1.80e-16	0.4	⋯	⋯	1.16e-14	3.79e-16	0.5	⋯	⋯
IRAS04303	148.	2.5	0.9	⋯	⋯	1.4	1.55e-15	4.00e-15	9.69e-15	3.58e-16	2.1	1.38e-14	8.42e-16
IRS48	125.	1.5	1.5	⋯	⋯	2.2	2.33e-16	1.38e-15	2.62e-15	4.15e-17	⋯	⋯	⋯
ISO-Oph204	167.	5.3	1.0	⋯	⋯	2.0	1.33e-14	1.76e-16	1.32e-13	4.01e-16	⋯	⋯	⋯
KKOphA	221.	7.5	5.1	⋯	⋯	6.8	−7.50e-18	1.55e-15	−4.43e-15	1.40e-15	⋯	⋯	⋯
KKOphB	221.	⋯	⋯	⋯	⋯	⋯	−3.27e-15	9.50e-15	⋯	⋯	⋯	⋯	⋯
LkHa330	308.	5.2	1.1	⋯	⋯	1.4	1.85e-18	8.74e-16	1.16e-14	1.82e-16	0.5	⋯	⋯
MWC297	408.	⋯	895.1	⋯	⋯	950.9	8.41e-17	1.07e-16	⋯	⋯	⋯	⋯	⋯
MWC480	155.	4.1	3.5	⋯	⋯	4.6	9.96e-18	9.02e-16	1.23e-14	6.94e-17	⋯	⋯	⋯
MWC758	155.	5.8	4.1	⋯	⋯	4.9	5.18e-17	7.54e-16	1.92e-14	8.99e-17	3.2	⋯	⋯
PDS156	398.	3.6	1.6	⋯	⋯	1.6	1.46e-17	2.38e-15	2.01e-14	2.74e-16	⋯	⋯	⋯
PDS520	375.	9.0	1.1	⋯	⋯	1.4	1.59e-16	5.04e-15	2.08e-14	5.27e-16	⋯	⋯	⋯
RCrA	95.	⋯	395.4	⋯	⋯	544.7	⋯	⋯	⋯	⋯	⋯	4.05e-18	2.10e-16
RNO90	117.	3.2	2.7	9.59e-15	1.25e-15	3.9	4.88e-15	1.09e-16	1.20e-13	1.71e-16	2.2	6.74e-15	5.96e-16
RULup	159.	6.4	1.2	3.50e-14	4.91e-15	1.7	8.35e-15	2.27e-16	1.20e-13	3.17e-16	4.4	2.62e-15	3.44e-16
RWAur	163.	⋯	1.0	⋯	⋯	1.4	⋯	⋯	⋯	⋯	1.5	−6.09e-15	4.82e-15
RYLup	158.	8.0	1.0	⋯	⋯	1.3	5.66e-18	5.20e-15	2.08e-14	5.50e-16	0.9	⋯	⋯
RYTau	444.	3.8	6.2	⋯	⋯	7.8	5.13e-16	1.77e-15	8.96e-15	1.43e-16	10.1	⋯	⋯
SCrAN	152.	7.3	⋯	⋯	⋯	⋯	⋯	⋯	4.47e-14	6.07e-17	28.0	4.09e-16	7.65e-16
SCrAS	168.	⋯	⋯	⋯	⋯	⋯	⋯	⋯	⋯	⋯	⋯	9.37e-16	3.90e-15

Table 4
(Continued)

Object	Dist	S	2.9 μm			5 μm					12.4 μm		
			F_c	F_{cn}	err	F_c	F_{cn}	err	F_{cn}(CO)	err(CO)	F_c	F_{cn}	err
SR21	138.	2.3	1.1	1.57e-16	1.62e-16	1.1	2.79e-16	8.88e-16	4.70e-15	1.10e-16	2.0	⋯	⋯
SR4	134.	3.9	1.0	⋯	⋯	0.8	8.38e-16	5.72e-15	6.22e-14	7.00e-16	0.8	⋯	⋯
SR9	130.	3.9	0.7	⋯	⋯	0.7	6.07e-16	6.87e-15	3.30e-14	7.60e-16	0.5	⋯	⋯
SUAur	158.	3.8	2.6	⋯	⋯	2.8	−1.20e-18	1.10e-15	7.65e-15	1.14e-16	2.2	⋯	⋯
TCrA	⋯	⋯	0.5	⋯	⋯	1.0	−8.77e-17	9.01e-16	⋯	⋯	⋯	3.08e-16	8.11e-16
TTauN	144.	6.1	2.2	5.77e-14	4.64e-14	10.0	⋯	⋯	3.82e-14	1.04e-16	⋯	⋯	⋯
TTauS	144.	⋯	2.2	4.45e-14	3.56e-14	10.0	⋯	⋯	⋯	⋯	⋯	⋯	⋯
TWCha	184.	4.6	0.2	2.38e-14	1.84e-16	0.2	⋯	⋯	6.85e-14	1.26e-15	0.1	⋯	⋯
TWHya	60.	2.8	0.5	4.29e-16	4.36e-16	0.3	2.42e-20	1.46e-15	2.50e-14	1.89e-16	0.5	⋯	⋯
UYAurA	155.	10.9	1.1	⋯	⋯	1.6	7.44e-15	2.29e-16	4.22e-14	3.15e-16	⋯	⋯	⋯
UYAurB	155.	3.7	1.1	⋯	⋯	1.6	6.73e-16	6.73e-15	2.14e-15	6.48e-15	⋯	⋯	⋯
V1331Cyg	587.	10.7	0.4	⋯	⋯	0.6	3.49e-15	1.75e-16	4.58e-14	4.48e-16	1.0	⋯	⋯
V1647Ori	451.	⋯	0.9	⋯	⋯	1.9	⋯	⋯	⋯	⋯	⋯	8.21e-16	1.77e-15
V853Oph	83.	⋯	0.4	⋯	⋯	0.4	⋯	⋯	⋯	⋯	0.5	4.65e-15	1.50e-14
V892Tau	117.	3.8	2.7	⋯	⋯	3.9	9.67e-17	4.02e-16	3.93e-14	3.31e-17	⋯	⋯	⋯
VVCrAN	149.	⋯	2.7	⋯	⋯	3.5	⋯	⋯	⋯	⋯	⋯	9.65e-16	8.90e-16
VVCrAS	149.	11.0	2.7	⋯	⋯	3.5	⋯	⋯	3.52e-14	4.22e-17	5.7	1.56e-15	1.14e-16
VVSer	403.	1.8	2.6	⋯	⋯	3.8	4.17e-17	5.46e-16	9.48e-15	1.09e-16	3.7	−1.17e-15	1.09e-15
VWCha	190.	5.9	1.2	1.67e-14	8.77e-16	1.3	⋯	⋯	1.23e-13	2.30e-16	0.8	1.80e-14	1.25e-15
VZCha	191.	4.0	0.4	1.87e-14	2.16e-16	0.4	⋯	⋯	1.11e-13	6.31e-16	0.4	⋯	⋯
WaOph6	123.	3.7	1.0	2.64e-14	1.85e-15	1.0	7.77e-16	7.30e-15	1.71e-14	5.01e-16	0.8	5.34e-16	2.89e-15
WXCha	190.	2.7	0.4	1.13e-14	3.77e-16	0.4	⋯	⋯	8.33e-14	1.21e-15	0.3	1.92e-14	2.41e-14

Note. Line fluxes and errors F_{cn} are in units of erg s^{-1} cm^{-2} Jy^{-1}, and continuum fluxes F_c are in janskys. Unless indicated in parentheses, the line flux and error refer to the water line at spectral wavelengths indicated at the top of the table (see Section 4.2 for the identification of lines at each wavelength). The CO line shape parameter S is reported in the third column for reference (for its definition, see Banzatti et al. 2022).

(This table is available in machine-readable form.)

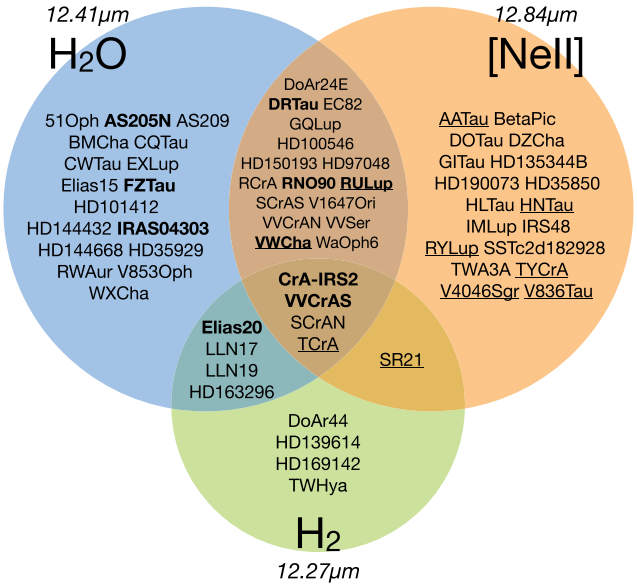

Figure 23. Venn diagram showing spectral settings and sample obtained in the VISIR survey included in this work. Detections are shown in boldface for water (presented in this work), and underlined for [Ne II] (presented in Pascucci et al. 2020). No detections are reported for H_2.

Table 5
Water Line Flux Measurements from *M*-band iSHELL Spectra

Line ID v (u-l) $J_{K_aK_c}$ (u-l)	Wavelength (μm)	AS 205 N		DR Tau		FZ Tau		CrA-IRS 2	
		F_{cn}	err	F_{cn}	err	F_{cn}	err	F_{cn}	err
1-0 $13_{7\,6}-12_{6\,7}$	4.52474	9.06e-15	1.77e-14	2.15e-15	1.13e-14	1.90e-15	1.79e-14	2.43e-16	1.85e-14
1-0 $9_{9\,0}-8_{8\,1}$	4.53470	4.82e-15	1.67e-14	1.66e-15	1.18e-14	1.46e-14	1.70e-14	3.86e-15	1.86e-14
1-0 $10_{8\,3}-9_{7\,2}$	4.57264	3.42e-15	8.60e-15	3.60e-15	9.28e-15	4.98e-15	1.50e-14	3.80e-15	1.10e-14
1-0 $12_{7\,6}-11_{6\,5}$	4.57608	3.88e-15	4.67e-15	2.62e-15	6.17e-15	3.43e-15	8.04e-15	3.81e-15	4.96e-15
1-0 $13_{6\,7}-12_{5\,8}$	4.61395	1.84e-16	2.25e-15	1.93e-16	1.39e-15	3.08e-16	2.62e-15	2.35e-16	1.53e-15
1-0 $11_{7\,4}-10_{6\,5}$	4.62229	5.23e-15	3.66e-16	1.64e-15	2.59e-16	5.70e-15	4.23e-16	3.15e-15	3.71e-16
1-0 $9_{7\,2}-8_{6\,3}$	4.72810	1.01e-14	1.07e-15	5.31e-15	5.28e-16	1.47e-14	1.36e-15	7.74e-15	1.10e-15
1-0 $11_{6\,5}-10_{5\,6}$	4.72942	7.34e-15	7.45e-16	3.48e-15	3.22e-16	1.16e-14	5.67e-16	7.14e-15	8.04e-16
1-0 $10_{6\,5}-9_{5\,4}$	4.79063	7.67e-15	7.78e-16	4.37e-15	4.57e-15	1.73e-14	1.39e-15	8.73e-15	7.73e-16
1-0 $18_{4\,15}-17_{3\,14}$	4.87733	5.81e-15	6.52e-15	1.09e-15	1.80e-15	6.88e-15	5.21e-16	1.90e-15	6.31e-15
1-0 $20_{3\,18}-19_{2\,17}$	4.88205	4.09e-15	3.31e-16	1.55e-15	1.81e-15	5.43e-15	5.02e-16	3.00e-15	2.44e-16
2-1 $7_{6\,1}-6_{5\,2}$	4.93554	3.59e-15	4.89e-15	1.80e-16	2.21e-15	3.89e-15	4.18e-15	3.50e-15	4.93e-15
2-1 $9_{5\,4}-8_{4\,5}$	4.95058	3.14e-15	4.41e-16	1.79e-16	3.15e-15	3.94e-15	6.09e-15	2.42e-15	3.40e-16
1-0 $16_{4\,13}-15_{3\,12}$	4.96548	3.98e-15	3.05e-16	2.41e-15	3.19e-16	8.20e-15	5.14e-16	2.41e-15	2.30e-16
1-0 $15_{4\,12}-14_{3\,11}$	5.00798	1.02e-15	2.51e-15	6.17e-16	1.86e-15	5.29e-15	5.52e-16	3.50e-15	2.52e-16
1-0 $17_{3\,15}-16_{2\,14}$	5.01522	1.69e-16	3.35e-15	1.76e-16	5.71e-15	2.85e-16	1.02e-14	2.20e-16	2.92e-15
1-0 $14_{4\,11}-13_{3\,10}$	5.04712	1.16e-14	4.30e-16	1.75e-16	2.24e-15	2.83e-16	4.05e-15	1.57e-14	3.31e-16
1-0 $23_{0\,23}-22_{1\,22}$	5.05889	1.01e-15	2.62e-15	1.50e-15	5.51e-15	1.69e-15	8.17e-15	7.57e-16	1.83e-15
1-0 $15_{4\,11}-14_{5\,10}$	5.05986	4.34e-15	6.73e-16	1.48e-15	5.77e-15	5.27e-15	1.32e-14	1.83e-15	3.95e-15
1-0 $16_{3\,14}-15_{2\,13}$	5.06240	7.30e-15	3.57e-16	4.56e-15	3.22e-16	1.22e-14	5.19e-16	7.79e-15	2.66e-16
1-0 $16_{2\,14}-15_{3\,13}$	5.06429	4.76e-15	3.28e-16	2.35e-15	3.27e-16	5.21e-15	5.16e-16	5.05e-15	2.30e-16
2-1 $7_{5\,2}-6_{4\,3}$	5.07548	3.92e-15	4.14e-16	2.36e-15	2.63e-15	8.00e-15	7.34e-16	7.24e-15	3.30e-16
1-0 $12_{4\,9}-11_{3\,8}$	5.10815	1.30e-14	8.01e-16	6.29e-15	4.80e-16	1.99e-14	8.55e-16	1.36e-14	9.14e-16
2-1 $16_{3\,14}-15_{2\,13}$	5.12485	3.86e-15	4.57e-16	2.77e-15	3.81e-15	8.63e-15	9.75e-15	8.69e-15	3.71e-16
1-0 $11_{4\,8}-10_{3\,7}$	5.13018	1.09e-14	1.03e-15	1.73e-16	3.85e-15	1.56e-14	1.19e-15	2.00e-14	1.25e-15
1-0 $14_{3\,12}-13_{2\,11}$	5.16010	4.24e-15	4.52e-15	4.44e-15	5.26e-16	5.80e-15	8.63e-16	2.33e-15	4.31e-15
1-0 $20_{1\,20}-19_{0\,19}$	5.16471	5.50e-15	4.97e-16	5.75e-15	4.88e-16	1.35e-14	7.86e-16	4.97e-15	3.97e-16
1-0 $14_{2\,12}-13_{3\,11}$	5.16709	3.44e-15	3.74e-15	2.74e-15	2.88e-15	6.55e-15	8.35e-16	2.31e-15	2.97e-15
2-1 $15_{2\,13}-14_{3\,12}$	5.18489	2.61e-15	4.52e-15	4.02e-15	6.36e-16	7.14e-15	1.02e-15	6.56e-15	4.55e-16
1-0 $13_{3\,10}-12_{4\,9}$	5.18710	1.04e-14	9.59e-16	1.71e-16	4.35e-15	5.13e-15	8.60e-15	1.17e-14	1.01e-15
2-1 $5_{5\,0}-4_{4\,1}$	5.20586	9.56e-15	1.02e-14	2.28e-15	8.82e-15	9.61e-16	1.84e-14	7.04e-15	1.51e-14
1-0 $15_{1\,14}-14_{2\,13}$	5.22140	1.46e-14	1.77e-15	1.41e-14	1.12e-15	3.32e-14	1.94e-15	1.33e-14	1.38e-14
1-0 $13_{2\,11}-12_{3\,10}$	5.22307	9.86e-15	1.29e-15	6.96e-15	1.08e-15	2.52e-14	1.94e-15	9.57e-15	1.51e-15
2-1 $14_{3\,12}-13_{2\,11}$	5.22645	5.03e-15	5.88e-15	2.28e-15	5.26e-15	8.52e-15	1.05e-14	2.83e-15	5.11e-15

Note. Line flux measurements have the same definition as in Table 4. A complete compilation of line fluxes and upper limits for all spectra included in this paper is available upon request to the first author.

(This table is available in machine-readable form.)

ORCID iDs

Andrea Banzatti https://orcid.org/0000-0003-4335-0900
Klaus M. Pontoppidan https://orcid.org/0000-0001-7552-1562
Colette Salyk https://orcid.org/0000-0003-3682-6632
Gregory J. Herczeg https://orcid.org/0000-0002-7154-6065
Ilaria Pascucci https://orcid.org/0000-0001-7962-1683
Sean Brittain https://orcid.org/0000-0001-5638-1330
Ewine F. van Dishoeck https://orcid.org/0000-0001-7591-1907
Inga Kamp https://orcid.org/0000-0001-7455-5349
Arthur D. Bosman https://orcid.org/0000-0003-4001-3589
Karin I. Öberg https://orcid.org/0000-0001-8798-1347
Geoff A. Blake https://orcid.org/0000-0003-0787-1610
Michael R. Meyer https://orcid.org/0000-0003-1227-3084
Eric Gaidos https://orcid.org/0000-0002-5258-6846
Adwin Boogert https://orcid.org/0000-0001-9344-0096
Caleb Wheeler https://orcid.org/0000-0001-5563-6987

References

Acke, B., Verhoelst, T., van den Ancker, M. E., et al. 2008, A&A, 485, 209
Agúndez, M., Roueff, E., Le Petit, F., & Le Bourlot, J. 2018, A&A, 616, A19
Alecian, E., Wade, G. A., Catala, C., et al. 2013, MNRAS, 429, 1001
Anderson, D. E., Blake, G. A., Cleeves, L. I., et al. 2021, ApJ, 909, 55
Andrews, S. M., Huang, J., Pérez, L. M., et al. 2018, ApJL, 869, L41
Antonellini, S., Kamp, I., Riviere-Marichalar, P., et al. 2015, A&A, 582, A105
Bailer-Jones, C. A. L., Rybizki, J., Fouesneau, M., Mantelet, G., & Andrae, R. 2018, AJ, 156, 58
Banzatti, A. 2013, PhD thesis, Eidgenossische Technische Hochschule, Zurich, Switzerland
Banzatti, A., Abernathy, K. M., Brittain, S., et al. 2022, AJ, 163, 174
Banzatti, A., Garufi, A., Kama, M., et al. 2018, A&A, 609, L2
Banzatti, A., Meyer, M. R., Bruderer, S., et al. 2012, ApJ, 745, 90
Banzatti, A., Meyer, M. R., Manara, C. F., Pontoppidan, K. M., & Testi, L. 2014, ApJ, 780, 26
Banzatti, A., Pascucci, I., Bosman, A. D., et al. 2020, ApJ, 903, 124
Banzatti, A., Pascucci, I., Edwards, S., et al. 2019, ApJ, 870, 76
Banzatti, A., & Pontoppidan, K. M. 2015, ApJ, 809, 167
Banzatti, A., Pontoppidan, K. M., Bruderer, S., Muzerolle, J., & Meyer, M. R. 2015, ApJL, 798, L16
Banzatti, A., Pontoppidan, K. M., Salyk, C., et al. 2017, ApJ, 834, 152

Bast, J. E., Brown, J. M., Herczeg, G. J., van Dishoeck, E. F., & Pontoppidan, K. M. 2011, A&A, 527, A119
Bitner, M. A., Richter, M. J., Lacy, J. H., et al. 2008, ApJ, 688, 1326
Blevins, S. M., Pontoppidan, K. M., Banzatti, A., et al. 2016, ApJ, 818, 22
Bosman, A. D., Bergin, E. A., Calahan, J., & Duval, S. E. 2022, ApJL, 930, L26
Bosman, A. D., Bruderer, S., & van Dishoeck, E. F. 2017, A&A, 601, A36
Brittain, S. D., Najita, J. R., Carr, J. S., et al. 2013, ApJ, 767, 159
Brittain, S. D., Najita, J. R., Carr, J. S., Ádámkovics, M., & Reynolds, N. 2016, ApJ, 830, 112
Brittain, S. D., Rettig, T. W., Simon, T., et al. 2003, ApJ, 588, 535
Brittain, S. D., Simon, T., Najita, J. R., & Rettig, T. W. 2007, ApJ, 659, 685
Brown, J. M., Blake, G. A., Dullemond, C. P., et al. 2007, ApJL, 664, L107
Brown, J. M., Herczeg, G. J., Pontoppidan, K. M., & van Dishoeck, E. F. 2012, ApJ, 744, 116
Brown, J. M., Pontoppidan, K. M., van Dishoeck, E. F., et al. 2013, ApJ, 770, 94
Carmona, A., van den Ancker, M. E., Henning, T., et al. 2008, A&A, 477, 839
Carr, J. S., & Najita, J. R. 2008, Sci, 319, 1504
Carr, J. S., & Najita, J. R. 2011, ApJ, 733, 102
Carr, J. S., Tokunaga, A. T., & Najita, J. 2004, ApJ, 603, 213
Ciesla, F. J., & Cuzzi, J. N. 2006, Icar, 181, 178
Cushing, M. C., Vacca, W. D., & Rayner, J. T. 2004, PASP, 116, 362
Cutri, R. M., Wright, E. L., Conrow, T., et al. 2021, yCat, II/328
Doppmann, G. W., Najita, J. R., Carr, J. S., & Graham, J. R. 2011, ApJ, 738, 112
Du, F., & Bergin, E. A. 2014, ApJ, 792, 2
Du, F., Bergin, E. A., Hogerheijde, M., et al. 2017, ApJ, 842, 98
Dubernet, M. L., Daniel, F., Grosjean, A., & Lin, C. Y. 2009, A&A, 497, 911
Dullemond, C. P., & Dominik, C. 2004, A&A, 417, 159
Dunkin, S. K., Barlow, M. J., & Ryan, S. G. 1997, MNRAS, 286, 604
Fang, M., Pascucci, I., Edwards, S., et al. 2018, ApJ, 868, 28
Faure, A., & Josselin, E. 2008, A&A, 492, 257
Fedele, D., Bruderer, S., van Dishoeck, E. F., et al. 2012, A&A, 544, L9
Fedele, D., Pascucci, I., Brittain, S., et al. 2011, ApJ, 732, 106
Finzi, J., Hovis, F. E., Panfilov, V. N., Hess, P., & Moore, C. B. 1977, JChPh, 67, 4053
Furlan, E., Watson, D. M., McClure, M. K., et al. 2009, ApJ, 703, 1964
Glassgold, A. E., Meijerink, R., & Najita, J. R. 2009, ApJ, 701, 142
Goldsmith, P. F., & Langer, W. D. 1999, ApJ, 517, 209
Gordon, I. E., Rothman, L. S., Hargreaves, R. J., et al. 2022, J. Quant. Spec. Radiat. Transf., 277, 107949
Guzmán-Díaz, J., Mendigutía, I., Montesinos, B., et al. 2021, A&A, 650, A182
Hartmann, L., Hewett, R., Stahler, S., & Mathieu, R. D. 1986, ApJ, 309, 275
Hein Bertelsen, R. P., Kamp, I., van der Plas, G., et al. 2016a, A&A, 590, A98
Hein Bertelsen, R. P., Kamp, I., van der Plas, G., et al. 2016b, MNRAS, 458, 1466
Herczeg, G. J., Brown, J. M., van Dishoeck, E. F., & Pontoppidan, K. M. 2011, A&A, 533, A112
Herczeg, G. J., & Hillenbrand, L. A. 2014, ApJ, 786, 97
Herczeg, G. J., Karska, A., Bruderer, S., et al. 2012, A&A, 540, A84
Huang, J., Andrews, S. M., Dullemond, C. P., et al. 2018, ApJL, 869, L42
Hunter, J. D. 2007, CSE, 9, 90
James, M. M., Pascucci, I., Liu, Y., et al. 2022, ApJ, 941, 187
Kaeufl, H.-U., Ballester, P., Biereichel, P., et al. 2004, Proc. SPIE, 5492, 1218
Kamp, I., Honda, M., Nomura, H., et al. 2021, PASA, 38, e055
Kamp, I., Thi, W. F., Meeus, G., et al. 2013, A&A, 559, A24
Käufl, H. U., Kerber, F., Asmus, D., et al. 2015, Msngr, 159, 15
Krijt, S., Kama, M., McClure, M., et al. 2022, arXiv:2203.10056
Kurtovic, N. T., Pérez, L. M., Benisty, M., et al. 2018, ApJL, 869, L44
Labdon, A., Kraus, S., Davies, C. L., et al. 2019, A&A, 627, A36
Labiano, A., Argyriou, I., Álvarez-Márquez, J., et al. 2021, A&A, 656, A57
Lacy, J. H., Richter, M. J., Greathouse, T. K., Jaffe, D. T., & Zhu, Q. 2002, PASP, 114, 153
Lagage, P. O., Pel, J. W., Authier, M., et al. 2004, Msngr, 117, 12
Larsson, B., Liseau, R., & Men'shchikov, A. B. 2002, A&A, 386, 1055
Liu, T., Zhang, H., Wu, Y., Qin, S.-L., & Miller, M. 2011, ApJ, 734, 22
Liu, Y., Pascucci, I., & Henning, T. 2019, A&A, 623, A106
Long, F., Andrews, S. M., Vega, J., et al. 2021, ApJ, 915, 131
Long, F., Pinilla, P., Herczeg, G. J., et al. 2018, ApJ, 869, 17
Manara, C. F., Tazzari, M., Long, F., et al. 2019, A&A, 628, A95
Mandell, A. M., Bast, J., van Dishoeck, E. F., et al. 2012, ApJ, 747, 92
Markwardt, C. B. 2009, in ASP Conf. Ser. 411, Astronomical Data Analysis Software and Systems XVIII, ed. D. A. Bohlender, D. Durand, & P. Dowler, 251
Meijerink, R., Pontoppidan, K. M., Blake, G. A., Poelman, D. R., & Dullemond, C. P. 2009, ApJ, 704, 1471
Mundt, R., & Eislöffel, J. 1998, AJ, 116, 860
Najita, J., Carr, J. S., & Mathieu, R. D. 2003, ApJ, 589, 931
Najita, J. R., Ádámkovics, M., & Glassgold, A. E. 2011, ApJ, 743, 147
Najita, J. R., Carr, J. S., Pontoppidan, K. M., et al. 2013, ApJ, 766, 134
Najita, J. R., Carr, J. S., Salyk, C., et al. 2018, ApJ, 862, 122
Notsu, S., Nomura, H., Ishimoto, D., et al. 2016, ApJ, 827, 113
Panić, O., Haworth, T. J., Petr-Gotzens, M. G., et al. 2021, MNRAS, 501, 4317
Panoglou, D., Cabrit, S., Pineau Des Forêts, G., et al. 2012, A&A, 538, A2
Pascucci, I., Banzatti, A., Gorti, U., et al. 2020, ApJ, 903, 78
Pascucci, I., Herczeg, G., Carr, J. S., & Bruderer, S. 2013, ApJ, 779, 178
Pascucci, I., & Sterzik, M. 2009, ApJ, 702, 724
Perez Chavez, J. A., Banzatti, A., Wheeler, C., & Pontoppidan, K. 2021, AAS Meeting Abstracts, 115.05
Pinilla, P., Tazzari, M., Pascucci, I., et al. 2018, ApJ, 859, 32
Pontoppidan, K. M., Bergin, E. A., Melnick, G., et al. 2018, arXiv:1804.00743
Pontoppidan, K. M., Blake, G. A., & Smette, A. 2011, ApJ, 733, 84
Pontoppidan, K. M., Meijerink, R., Dullemond, C. P., & Blake, G. A. 2009, ApJ, 704, 1482
Pontoppidan, K. M., Salyk, C., Blake, G. A., & Käufl, H. U. 2010b, ApJL, 722, L173
Pontoppidan, K. M., Salyk, C., Blake, G. A., et al. 2010a, ApJ, 720, 887
Prato, L., Greene, T. P., & Simon, M. 2003, ApJ, 584, 853
Rab, C., Weber, M., Grassi, T., et al. 2022, A&A, 668, A154
Rayner, J., Tokunaga, A., Jaffe, D., et al. 2016, Proc. SPIE, 9908, 990884
Rayner, J., Tokunaga, A., Jaffe, D., et al. 2022, PASP, 134, 015002
Rieke, G. H., Wright, G. S., Böker, T., et al. 2015, PASP, 127, 584
Riviere-Marichalar, P., Ménard, F., Thi, W. F., et al. 2012, A&A, 538, L3
Ros, K., & Johansen, A. 2013, A&A, 552, A137
Salyk, C., Blake, G. A., Boogert, A. C. A., & Brown, J. M. 2009, ApJ, 699, 330
Salyk, C., Blake, G. A., Boogert, A. C. A., & Brown, J. M. 2011a, ApJ, 743, 112
Salyk, C., Herczeg, G. J., Brown, J. M., et al. 2013, ApJ, 769, 21
Salyk, C., Lacy, J., Richter, M., et al. 2019, ApJ, 874, 24
Salyk, C., Pontoppidan, K. M., Banzatti, A., et al. 2022, AJ, 164, 136
Salyk, C., Pontoppidan, K. M., Blake, G. A., et al. 2008, ApJL, 676, L49
Salyk, C., Pontoppidan, K. M., Blake, G. A., Najita, J. R., & Carr, J. S. 2011b, ApJ, 731, 130
Sargent, B. A., Forrest, W., Watson, D. M., et al. 2014, ApJ, 792, 83
Schöier, F. L., van der Tak, F. F. S., van Dishoeck, E. F., & Black, J. H. 2005, A&A, 432, 369
Simon, M. N., Pascucci, I., Edwards, S., et al. 2016, ApJ, 831, 169
Sullivan, K., Prato, L., Edwards, S., Avilez, I., & Schaefer, G. H. 2019a, ApJ, 884, 28
Sullivan, T., Wilking, B. A., Greene, T. P., et al. 2019b, AJ, 158, 41
Tabone, B., Godard, B., Pineau des Forêts, G., Cabrit, S., & van Dishoeck, E. F. 2020, A&A, 636, A60
Tennyson, J., Zobov, N. F., Williamson, R., Polyansky, O. L., & Bernath, P. F. 2001, JPCRD, 30, 735
Thi, W. F., Kamp, I., Woitke, P., et al. 2013, A&A, 551, A49
Tripathi, A., Andrews, S. M., Birnstiel, T., & Wilner, D. J. 2017, ApJ, 845, 44
Ubeira Gabellini, M. G., Miotello, A., Facchini, S., et al. 2019, MNRAS, 486, 4638
van der Marel, N., van Dishoeck, E. F., Bruderer, S., et al. 2016, A&A, 585, A58
van der Plas, G., van den Ancker, M. E., Waters, L. B. F. M., & Dominik, C. 2015, A&A, 574, A75
van der Tak, F. F. S., Black, J. H., Schöier, F. L., Jansen, D. J., & van Dishoeck, E. F. 2007, A&A, 468, 627
van Dishoeck, E. F., Bergin, E. A., Lis, D. C., & Lunine, J. I. 2014, in Protostars and Planets VI, ed. Planets et al. (Tucson, AZ: Univ. Arizona Press), 835
Walsh, C., Nomura, H., & van Dishoeck, E. 2015, A&A, 582, A88
Wang, L., Bai, X.-N., & Goodman, J. 2019, ApJ, 874, 90
Waskom, M. 2021, JOSS, 6, 3021
Wichittanakom, C., Oudmaijer, R. D., Fairlamb, J. R., et al. 2020, MNRAS, 493, 234
Woitke, P., Min, M., Pinte, C., et al. 2016, A&A, 586, A103
Woitke, P., Min, M., Thi, W. F., et al. 2018, A&A, 618, A57
Wölfer, L., Facchini, S., Kurtovic, N. T., et al. 2021, A&A, 648, A19
Wu, Y., Wei, Y., Zhao, M., et al. 2004, A&A, 426, 503
Yang, Y.-L., Green, J. D., Pontoppidan, K. M., et al. 2022, ApJL, 941, L13
Yvart, W., Cabrit, S., Pineau des Forêts, S., & Ferreira, S. 2016, A&A, 585, A74